SAND2019-3875C

Using Chemical Kinetics to Understand Effects of Fuel Type and Compression Ratio on Knock-Mitigation Effectiveness of Various EGR Constituents

Namho Kim, David Vuilleumier, Magnus Sjöberg
Sandia National Laboratories

Nozomi Yokoo, Terutoshi Tomoda, Koichi Nakata
Toyota Motor Corp

Abstract

Exhaust gas recirculation (EGR) can be used to mitigate knock in SI engines. However, experiments have shown that the effectiveness of various EGR constituents to suppress knock varies with fuel type and compression ratio (CR). To understand some of the underlying mechanisms by which fuel composition, octane sensitivity (S), and CR affect the knock-mitigation effectiveness of EGR constituents, the current paper presents results from a chemical-kinetics modeling study. The numerical study was conducted with CHEMKIN, imposing experimentally acquired pressure traces on a closed reactor model. Simulated conditions include combinations of three RON-98 (Research Octane Number) fuels with two octane sensitivities and distinctive compositions, three EGR diluents, and two CRs (12:1 and 10:1). The experimental results point to the important role of thermal stratification in the end-gas to smooth peak heat-release rate (HRR) and prevent acoustic noise. To model the effects of thermal stratification due to heat-transfer losses to the combustion-chamber walls, the initial temperature at the start of the CHEMKIN simulation was successively reduced below the adiabatic core temperature while observing changes in end-gas heat release and its effect on the reactant temperature.

The results reveal that knock-prone conditions generally exhibit an increased amount of heat release in the colder temperature zones, thus counteracting the HRR-smoothing effect of the naturally occurring thermal stratification. This detrimental effect becomes more pronounced for the low-S fuel due to its significant Negative Temperature Coefficient (NTC) autoignition characteristics. This explains the generally reduced effectiveness of dilution for the low-S fuel, and higher knock intensity for the cycles with autoignition.

Introduction

The use of external Exhaust Gas Recirculation (EGR) in spark-ignited (SI) engines has increased due to numerous merits for efficiency improvement [1-4]. Recently released engines are employing EGR rates above 20% to realize high thermal efficiency [3, 4]. EGR can improve thermal efficiency by reducing pumping losses at part-load conditions as intake pressure has to be increased to maintain the same amount of fresh charge. EGR also reduces the reactant temperature, especially during combustion, as a direct effect of charge dilution. The reduction of the reactant temperature reduces heat losses from the working fluid to the combustion-chamber walls, increases the specific heat ratio of the charge, and mitigates knock. For turbocharged engines, it is possible to minimize fuel enrichment at highly boosted conditions as EGR helps to keep exhaust gas temperatures below critical turbine inlet temperatures [5, 6]. To maximize merits arising from lowering the reactant temperature, EGR gasses are often cooled externally before introduction to the intake stream.

Investigations have previously been made on the effect of EGR on knock mitigation and how the effectiveness of EGR can change with variations in conditions. Kumano and Yamaoka [7] conducted a numerical study using a quasi-dimensional combustion model utilizing the Livengood-Wu integral for knock prediction at 4000 rpm, 130 kPa of intake pressure. The simulation results showed that increasing EGR rate by 1%-unit contributes to advancement of knock-limited combustion phasing (KL-CA50) by 0.5 degrees crank-angle (°CA) and reduction of fuel consumption by 0.4%. Experiments were also conducted using simulated EGR gas and showed that each % increment of EGR allows KL-CA50 to be advanced by 0.6°CA, confirming the simulation result. Szybist et al. [8] utilized chemical-kinetics modeling to understand changes in effectiveness of EGR on knock suppression under different operating conditions. Splitter and Szybist [9, 10] studied the effectiveness of EGR for knock suppression using a regular-grade gasoline fuel with anti-knock index (AKI) of 87 and two blends of alcohol and gasoline fuel which had higher AKI than 87. The results indicated that the effectiveness of EGR for knock suppression changes with fuels of different compositions and AKI ratings, and a gasoline-based fuel blended with 30% of ethanol by volume benefited the least from EGR. These examples highlight that there have been studies that quantify the knock-mitigation effectiveness of EGR, and how the effectiveness changes with engine operating conditions or fuel types. On the other hand, these previous studies did not investigate the knock-mitigation effects of individual EGR constituents.

EGR gases from stoichiometric mixtures of fuel and air include, but are not limited to, nitrogen (N_2), carbon dioxide (CO_2), water (H_2O), and trace species such as unburned hydrocarbon (UHC), carbon monoxide (CO), hydrogen (H_2) and nitric oxide (NO). N_2, CO_2, and H_2O have distinctly different heat capacity and specific heat ratios which affect compression heating effects during the compression stroke and combustion process [11]. Francqueville and Michel [12] carried out an experimental study using N_2, CO_2, or mixtures of the two gases to understand underlying mechanisms of EGR on knock mitigation. Based on the measured KL-CA50, the authors concluded that the thermal effect of diluents are more critical than chemical effects for knock suppression. The authors also attributed the higher heat capacity of CO_2 for its stronger knock mitigating effect compared to N_2. Unlike N_2 or CO_2, the effect of H_2O on knock suppression has been exploited by adding H_2O to the charge with a separate injector [13, 14]. Kim et al. [14] observed strong knock-suppressing effects of H_2O in a naturally-aspirated engine where H_2O was injected directly into the cylinder. The primary reason for the knock-suppressing effect of H_2O was attributed to high heat of vaporization (HoV) of H_2O, which cooled the unburned charge as it

evaporated. NO was identified as a knock-promotor from previous studies, although some studies reported that NO could reduce reactivity of the air-fuel mixture depending on the Negative Temperature Coefficient (NTC) behavior of the fuel [11, 15-17].

For better understanding of the effects of EGR constituents and the interactions with different fuel types, Vuilleumier et al. [18] conducted a study of individual and combined effects of EGR constituents on knock mitigation using compositionally dissimilar fuels at two CRs. A common baseline condition with matched combustion phasing was established to quantify the effectiveness of dilution. This approach was taken to minimize bias due to the temperature and pressure history of the end-gas, which can vary significantly when the combustion phasing is different, leading to a different response to diluent addition if the baseline conditions had different combustion phasings. The experiments revealed that, for most diluent/CR combinations, a fuel with low octane sensitivity (S) benefited less from dilution compared to two fuels with high S. Numerical investigations accompanied the experiments to provide a potential explanation of the reduced knock mitigation effect of CO_2 dilution at CR = 12, compared to CR = 10. The numerical study incorporated the concept of thermal stratification in the end-gas which affects the degree of sequential autoignition and could affect acoustic knock. The numerical study indicated that thermal stratification in the end-gas for that particular condition at CR = 10 was less affected by low-temperature heat release (LTHR) compared to the CR = 12 case, resulting in broader thermal stratification and more sequential autoignition, reducing the likelihood of acoustic knock.

Building from [18], the objective of the current study is to understand how knock-mitigation effectiveness of EGR constituents is affected by fuel composition, octane sensitivity, and CR using chemical-kinetics modeling. First, the concept of thermal stratification in the end-gas is employed, and the change in thermal stratification and autoignition timings of the baseline condition for three RON-98 fuels will be compared. Then, differences in effectiveness of diluents will be discussed. Lastly, the predicted differences in sequential autoignition will be tied to the experimental observation on statistics of knock intensity and provide a connection between the simulation results and the experimental data.

Experimental Hardware and Conditions

Numerical results in the current paper are well linked through comparisons and through the modeling methodology to experimental results presented in [18]. As the results presented in [18] inform the choices of conditions studied in this work, the experimental setup and conditions are briefly reiterated here. The preceding experiment used a directly-injected spark-ignition (DISI) four-valve single-cylinder research engine with an all-metal configuration. Two CRs were used: 12:1 and 10:1. The CR was adjusted through the alteration of the piston adapter plate explained in [18]. Figure 1 (a) and (b) show a cross section of the combustion chamber with the piston at top dead-center (TDC) for CR = 10 and 12, respectively. It can be seen that the squish height at TDC of higher CR is substantially smaller (4.8 mm vs 6.8 mm). Figure 1(c) presents the geometry of the piston crown to aid the interpretation of Figure 1(a) and (b). Other general specifications of the engine are provided in Table 1.

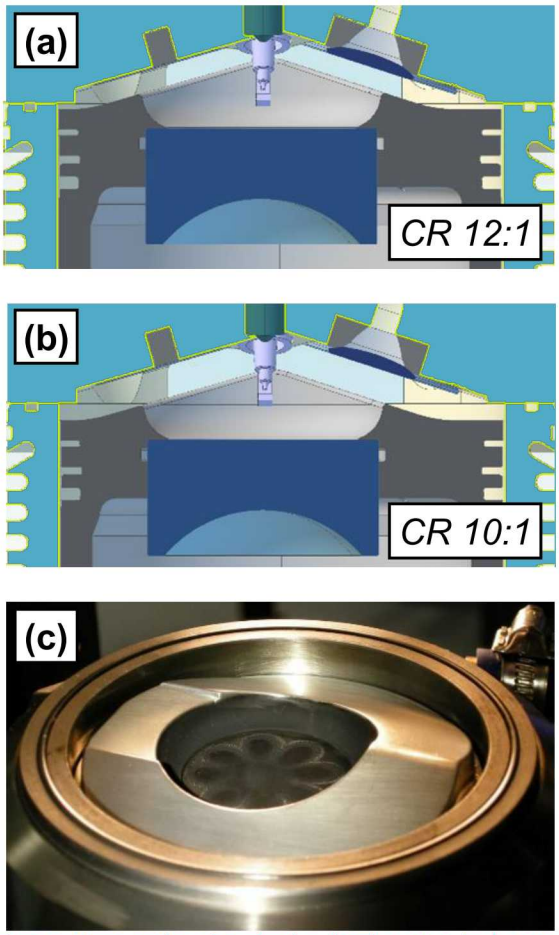

Figure 1. Cross section of combustion chamber at top dead-center for CR of (a) 12:1 and (b) 10:1. Geometry of the piston is shown in (c).

The engine speed was held constant at 1400 rpm, as controlled by an electric motor. Spark timing was set for each operating condition to achieve KL-CA50. KL-CA50 is defined as the average 50% burn point (CA50) over 500 cycles that corresponds to an average Knock Intensity (KI) level of 70 kPa. More details about the computation of KI values can be found in Appendix A and [18].

An intake temperature of 60 °C was used for all experiments. Working fluids, including air, N_2, and CO_2, were metered into the intake system using actively controlled sonic-flow nozzles. The fuel was injected using three equally spaced (20°CA) injections starting -310°CA after top dead-center (aTDC) to prepare a well-mixed in-cylinder charge. All of the following °CA values presented in this paper are aTDC.

Experiments were conducted at prescribed charge-mass based equivalence ratios (ϕ_m). The definition of ϕ_m may be found in Equation 1, where F, A, and C represent the intake-supplied mass of Fuel, Air, and gas Charge, respectively. The mass of gas charge, C, is the sum of all air and diluents. The baseline undiluted conditions used a ϕ_m of unity, while each diluent was tested at $\phi_m = 0.85$. For diluents which do not contain oxygen, such as N_2 and CO_2, the resulting fuel-air equivalence ratio (ϕ) was unity. When the diluents were added to the intake stream, the original air flow for the baseline condition was kept the same.

$$\phi_m \equiv \frac{\left(F/C\right)_{Actual}}{\left(F/A\right)_{Stoichiometric}} \quad (1)$$

For fair comparisons of the knock-mitigation benefit of different diluents across a range of three fuels and two CRs, a baseline operating condition was established for each fuel and CR combination. The baseline condition was set by adjusting the intake pressure such that KL-CA50 was equal to 20°CA at a fixed engine speed and intake temperature [18].

Table 1. General experimental engine specifications.

Displacement	0.552 liters
Bore	86.0 mm
Stroke	95.1 mm
Connecting Rod Length	166.7 mm
Geometric CR	10:1 or 12:1
Intake Valve Diameter	35.1 mm
Intake Valve Angle Relative to Cylinder Axis	18°
Exhaust Valve Diameter	30.1 mm
Exhaust Valve Angle Relative to Cylinder Axis	16°
Fuel Injector	Bosch 8-hole solenoid type
Fuel Injector Hole Orientation	Symmetric with 60° included angle
Fuel Injector Hole Size	Stepped-hole, minimum diameter = 0.125 mm

Numerical Study

Conditions of Interest

The numerical study was conducted using combinations of three fuels and two CRs, 12:1 and 10:1, for diluted and non-diluted conditions. Three types of diluents, namely air, N_2, and CO_2, are considered. In this study, only one dilution level is considered for each diluent. The selected dilution level for air, N_2, and CO_2 is $\phi_m = 0.85$. All the conditions were maintained to be stoichiometric except for the air-diluted condition where the ϕ changed with dilution level. Table 2 shows the resulting matrix of ϕ and ϕ_m for non-diluted and diluted conditions.

Table 3 lists key properties of the fuels used in this study. All three share a common Research Octane Number (RON ≈ 98), but vary in octane sensitivity (S) and composition. The Alkylate fuel has limited boiling range and consists mostly of saturated hydrocarbons. It has the lowest octane sensitivity among the fuels (S = 1.3). The High Aromatic and E30 fuels are both full-boiling range fuels with a high octane sensitivity, around S = 10.5. The high S stems from the relatively high content of aromatic and ethanol, respectively. Due to the high heat of vaporization (HoV) and low stoichiometric air-fuel ratio of ethanol, the E30 fuel has the highest HoV and charge-cooling properties per mass of stoichiometric charge among the fuels.

Figure 2 shows KL-CA50 measured for combinations of test fuels and diluents at two different CRs. The data were obtained from [18]. While the Alkylate fuel shows limited benefit from dilution for either CR, the CO_2-diluted condition at CR = 10 stands out as an exception to this statement. Modeling presented in [18] showed that a possible reason for the stronger knock-suppressing effect of CO_2 at CR = 10 is better utilization of thermal stratification in the end-gas to smooth the autoignition-based heat-release rate (HRR). Unlike for the Alkylate fuel, the knock-suppression effect of CO_2 and N_2 for the other fuels (with higher S) were significantly greater. Although dilution of the charge with CO_2 or N_2 had a positive effect in suppressing knock, dilution with air did not help suppress knock regardless of the fuel type nor CR. One of the goals of this study is to understand why the knock-suppression effectiveness of a diluent changes with fuel type as observed in Fig. 2.

Table 2 – Comparison of conventional equivalence ratio (ϕ) and mass-based equivalence ratio (ϕ_m) for various diluents.

Diluent	ϕ	ϕ_m
None (baseline)	1	1
Air	0.85	0.85
N_2, CO_2	1	0.85

Table 3. Selected fuel properties.

	Alkylate	High Aromatic	E30
RON (Research Octane Number)	98.0	98.1	97.9
MON (Motor Octane Number)	96.7	87.6	87.1
Octane Sensitivity, S (RON – MON)	1.3	10.5	10.8
Alkanes [vol.%]	98.8	46.2	40.5
Aromatics [vol.%]	0.7	39.8	13.8
Ethanol [vol.%]	0	0	30.6
Lower Heating Value [MJ/kg]	44.5	43.0	38.2
HoV per Mass of Stoichiometric Charge [kJ/kg]	19.1	23.3	38.3
Stoichiometric Air-Fuel Ratio	15.1	14.5	12.9

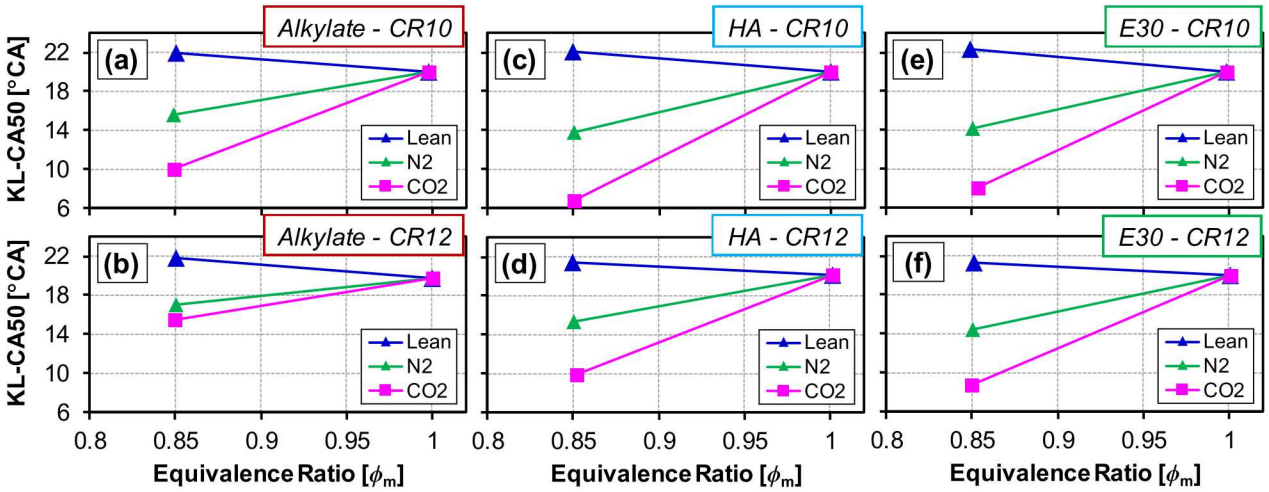

Figure 2. Experimentally measured KL-CA50 for Alkylate, High Aromatic, and E30 at CR = 10 and CR = 12 [18].

Methodology

The numerical study was conducted using the commercial software CHEMKIN-PRO [19]. A closed homogeneous reactor model was used, imposing experimentally acquired pressure traces to simulate conditions similar to that experienced by the end-gas in a real engine. For a knock-limited operating condition, the end-gas is compressed and heated until autoignition occurs due to the pressure rise associated with deflagration-based HRR and piston motion. The reasons for using this approach instead of utilizing a two-zone model for SI engines are explained in Appendix B.

In the experiment, in-cylinder pressure is measured over 500 consecutive cycles, and the average CA50 is adjusted by spark timing to match the target knock intensity as discussed in Appendix A, which provides details on the experimental procedures. Although the average knock intensity indicates that audible knock is detected, not all the cycles exhibit observable autoignition. To impose the condition that explicitly shows autoignition in the end-gas, 50 cycles with the most advanced CA50 were selected from the original data set, and in-cylinder pressure was averaged over the downsampled data. The CA50 was used as a criterion for downsampling because the cycles with advanced CA50 result in stronger autoignition in the end-gas [20].

The experimental autoignition timing was defined by the local-minimum point in the apparent heat-release rate (AHRR) that precedes the high rate of heat release near the end of combustion, as exemplified in Fig. 3 (a). The average autoignition timing was computed from the autoignition timings of individual cycles. The average burned mass fraction at the autoignition timing was determined from the location of the local-minimum point in the AHRR plotted against the burn points, as shown in Fig. 3 (b).

The starting points of the simulations are determined based on the timing when the experimentally based mass-averaged reactant temperature equals approximately 500 K for the baseline operating conditions. This modeling approach is utilized to reduce uncertainties in the inputs provided to the simulation, following the analyses in [21]. For the cases with the Alkylate and High Aromatic fuels, 500 K is reached at approximately -72.5°CA, which is used as the starting point for the simulations of these two fuels. However, for the E30 fuel, the charge temperature is lower due to its higher HoV, reaching 500 K around -68.9°CA, which is used as the starting point for the E30 simulations.

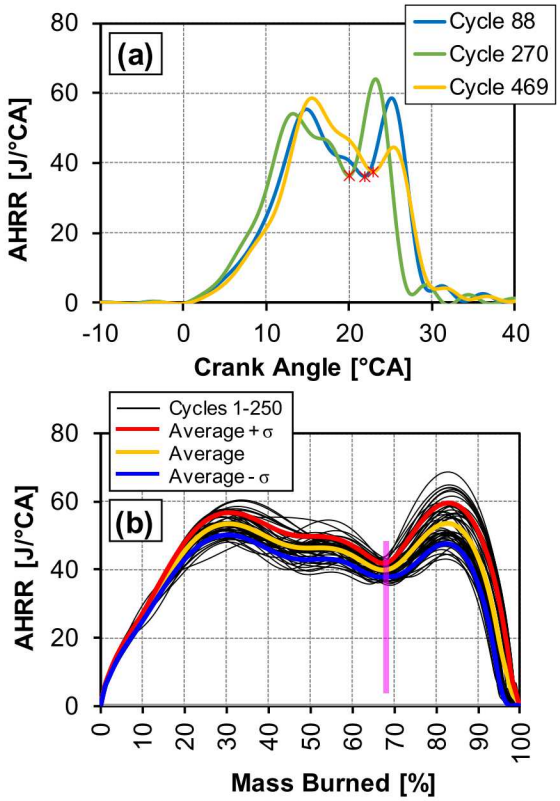

Figure 3. AHRR plotted against crank angle and burn points. The red markers in (a) highlight local-minimum points in AHRR which indicate the autoignition timing for individual cycles. The pink bar in (b) highlights the burned mass fraction that coincides with the local-minimum point.

At these crank angles, the in-cylinder charge is close to thermally uniform since very little heat-transfer losses to the cylinder wall have been incurred [22]. The CHEMKIN model does not directly incorporate heat transfer. Therefore, when the model is initiated with a temperature of 500 K and an experimental pressure trace is imposed, the resulting temperature corresponds to a fictional adiabatic core. In the experiment, the first autoignition is expected to

occur in this core [23]. However, the temperature in the real end-gas varies from that of the adiabatic core due to heat transfer from the end-gas to combustion-chamber walls as well as turbulent mixing in the thermal boundary layer [24]. In [25], thermal stratification in the end-gas is shown to play an important role in creating a sequential autoignition event which smooths the heat release rate due to autoignition. To model the effect of thermal stratification in the end-gas, multiple simulations were initialized with varying starting temperatures in -10 K steps from that of the adiabatic core temperature. Although the original simulation conditions included cases with initial temperatures 50 K lower than the adiabatic core temperature, the results presented here are limited to cases with initial temperatures of 40K lower than the adiabatic temperature to avoid considering any cases which do not autoignite.

The chemical mechanism used in this study is a detailed gasoline surrogate kinetic mechanism developed by Lawrence Livermore National Laboratory (LLNL). This mechanism contains 2871 species with 12804 reaction steps. This reaction mechanism also includes chemistry related to nitric oxide (NO) to consider the impact of NO on autoignition chemistry as reported in previous studies [15-17].

The surrogate formulations were also provided by LLNL, and these had been optimized with the kinetic mechanism to appropriately capture composition, distillation characteristics, and autoignition behavior in terms of RON and MON via ignition delay correlations [26]. The surrogate compositions of the test fuels are shown in Table 4.

Table 4. Chemical composition of the gasoline surrogate used in chemical-kinetics modeling [8].

Molecule Mole Fraction	Alkylate	High Aromatic	E30
n-butane	1.6%	6.7%	2.7%
1-hexene	0.0%	5.4%	3.9%
1,2,4-trimethylbenzene	2.3%	21.7%	5.5%
iso-pentane	0.0%	7.0%	6.5%
n-pentane	5.5%	10.5%	7.1%
n-heptane	0.0%	0.0%	8.0%
iso-octane	90.6%	34.6%	15.9%
toluene	0.0%	14.1%	0.0%
ethanol	0.0%	0.0%	50.5%

The composition of the simulated mixture is determined from measured mass flowrate of air and diluent into the intake system and amount of residual gas estimated by following the methodology explained in [27]. The amount of trace species, UHC, CO, NO, and nitrogen dioxide (NO_2), and combustion products, CO_2 and H_2O, in the residual gas are estimated based on the measurement of exhaust gas. It was assumed that the mixture is homogeneous in the end-gas and therefore, ϕ was set according to Table 2.

Contours of constant-volume ignition delays plotted in temperature and pressure space can provide insight into the autoignition process by visualizing changes in reactivity caused by different diluents. It is also useful to visualize which temperature-pressure (TP) regimes the end-gas reactants traverse for a given experimental condition, relative to the ignition delay behavior. Thus, ignition delay maps were generated based on constant-volume simulations for combinations of fuels and diluents, with TP trajectories overlaid. The constant-volume simulations were conducted in order to mimic the ignition delay measurements obtained with shock tubes and rapid compression machines. The constant-volume simulations were carried out by varying initial temperature from 650 K to 1000 K and initial pressure from 4 bar to 60 bar. Initial temperature and pressure were increased in steps of 10 K and 2 bar, respectively. NO was added to the mixture for ignition delay calculations to capture the effect of residual-trapped NO. Although the CR is not a variable for the computation of ignition delay map, the amount of NO varies with CR for the engine experiments. To compare the TP trajectories of two CRs on the same ignition delay map, the average amount of NO from two CRs were included in the mixture composition. Table 5 shows how the mole fraction of NO varies with fuel and diluent type for these ignition delay calculations.

A criterion is needed to determine the autoignition timings of the chemical-kinetics simulations. There are numerous criteria such as the time when the amount of hydroxyl radical (OH) present in the mixture reaches its maximum, the time at which temperature rise rate reaches its maximum value, or the time when the reactant temperature reaches 1500 K [19]. The time when the reactant temperature reaches 1500 K was found to correlate well with the time when the amount of OH reaches its peak in Ref. [19]. In this study, the influence of the criteria was investigated for a subset of conditions using the three criteria specified above. It was found that the timing when the temperature reaches 1500 K takes place earliest of the three. Despite some differences in predicted autoignition timings with different criteria, the comparison revealed that the maximum deviation in the predicted autoignition timing is less than 0.015 ms. This result converts to 0.13°CA as the experiment was conducted at an engine speed of 1400 rpm. This level of deviation is considered negligible because it is one order of magnitude lower than the deviation between the simulation results and experimental data which will be presented in the following section. Thus, in this study, the time when the reactant temperature reaches 1500 K is used as the criterion for determination of autoignition timing.

Table 5 – Mole fraction of NO (in ppm) for the computation of constant-volume ignition delay maps.

Diluent	Alkylate	High Aromatic	E30
None	95.3	100.4	90.7
Lean	107.6	126.3	104.9
N_2	37.6	49.1	41.2
CO_2	34.1	50.0	40.9

Simulation results

Autoignition Characteristics of Test Fuels

To illustrate the autoignition characteristics of the three test fuels, constant-volume ignition delay maps were calculated for stoichiometric mixtures without any diluents or trace species, as

presented in Fig. 4. The Alkylate fuel is the only fuel that exhibits strong NTC behavior, with the NTC region highlighted in Fig. 4(a). This supports previous findings in [8, 28] that fuels with lower octane sensitivity exhibit stronger NTC behavior than fuels with higher octane sensitivity. For the High Aromatic and E30 fuels, Figs. 4(b) and 4(c) highlight regimes of ignition delay with strongly reduced temperature sensitivity. This region of reduced temperature sensitivity is wider for the High Aromatic fuel compared to the E30 fuel, suggesting differences in autoignition chemistry despite having nearly identical RON and MON. The overall characteristics seen in Fig. 4 are consistent with the results presented in [8] where the authors used a previous version of the LLNL chemical mechanism and a different simulation tool.

Differences in the autoignition timing of the Alkylate and the High Aromatic fuels were compared by computing the ratios of ignition delays of the two fuels. Figure 5 presents the ratio of ignition delay times between the High Aromatic fuel and the Alkylate fuel. This figure shows that the High Aromatic fuel exhibits shorter ignition delay for temperatures higher than 800 K and pressures lower than 40 bar. However, for temperatures lower than 750 K, the High Aromatic fuel exhibits much longer ignition delays. This is due to the NTC behavior of the Alkylate fuel where reactivity increases with lower temperature. Despite very similar RON and MON values of the surrogates for the High Aromatic and E30 fuels, some differences were observed from the constant-volume ignition delay maps. Ratios of ignition delays of the High Aromatic and E30 fuels are shown in Fig. 6. Figure 6(a) shows the ratios of constant-volume ignition delays computed without any compensations for differences in HoV of the two fuels whereas Fig.6(b) shows the ratios computed with compensation for differences in HoV. The effect of HoV difference was computed based on the assumption that all of the cooling effect contributes to changing the reactant temperature prior to any reactions. Based on changes in the volumetric efficiency of the engine, it was estimated that the stoichiometric mixture of the E30 fuel had ~10 K lower temperature than that of the High Aromatic fuel. Based on this estimation, the ratio was computed by shifting the x-axis of the constant-volume ignition delay of the E30 fuel by 10 K. Figure 6 indicates that High Aromatic fuel has longer ignition delays compared to the E30 fuel at temperatures higher than 850 K regardless of pressure. Figure 6(b) shows that the difference in reactivity for higher temperature regime reduces significantly if the initial temperature is compensated for differences in HoV. Although the consideration on HoV effect reduced the differences between the ignition delays in the temperature regime higher than 850 K, the E30 fuel still exhibits shorter ignition delays compared to the High Aromatic fuel.

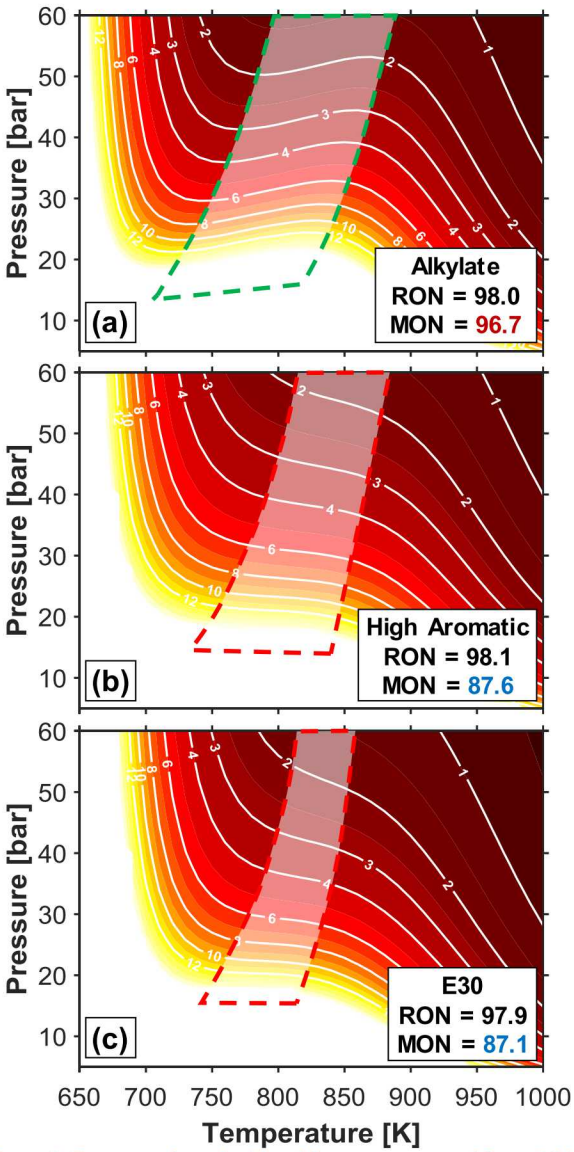

Figure 4. Constant-volume ignition delay maps computed for stoichiometric mixture of the (a) Alkylate, (b) High Aromatic, and (c) E30 fuels. Trace species such as NO is not included to the mixture. The regime which exhibit NTC (green) or reduced sensitivity to initial temperature (red) are highlighted.

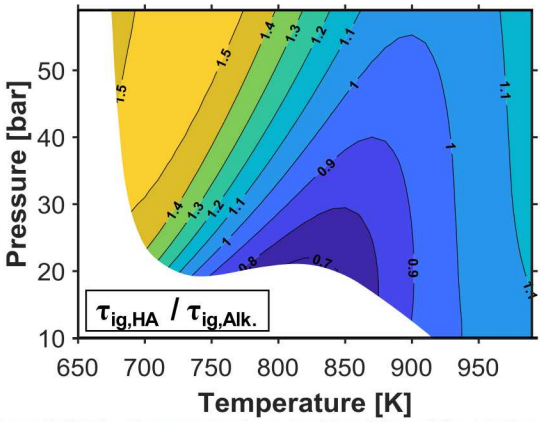

Figure 5. Ratio of constant-volume ignition delay of the Alkylate and the High Aromatic fuels.

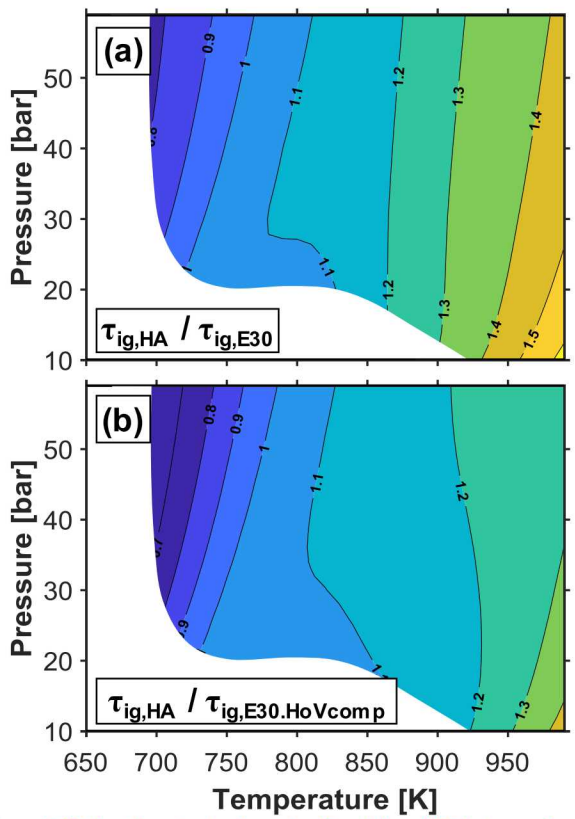

Figure 6. Ratio of constant-volume ignition delay of High Aromatic and E30 fuel for two scenarios: (a) without and (b) with compensation for differences in HoV.

Validation of end-gas autoignition modeling approach

The modeling approach used in this numerical study was validated for various conditions by comparing predicted autoignition timings with values measured experimentally following the methodology explained in the previous section. Figure 7 compares measured and predicted autoignition timings for undiluted and diluted conditions at the two CRs. The deviation between the experimentally observed and predicted autoignition timings is less than 1.9°CA for the Alkylate and E30 fuels, and less than 3°CA for the High Aromatic fuel. For comparison, the cycle-to-cycle variability of the downsampled experimental data equates to a standard deviation (σ) in autoignition timing in the range of 0.9 to 1.4°CA. Deviations in the prediction of autoignition timing can have several possible causes, including uncertainty in model inputs. The effect of uncertainty in the model inputs were quantified and explained in Appendix C. It was found that the combined effect of variation in the initial temperature, ϕ, and amount of NO by ±5 K, ±0.04, and ±10 ppm, respectively, shifted the predicted autoignition timing less than ±1°CA at CR = 12, undiluted condition for all three fuels. Figure 7 also shows that the shift in autoignition timing with CR is also well captured by the model. This indicates that the chemical mechanism responds accurately when fuel type and engine-operating conditions change, providing confidence in the model's ability to provide insights of the factors responsible for the experimentally observed trends. Overall, given the possible effects of uncertainty in inputs and experimental fluctuations in autoignition timing, the agreement between the model and experiments is considered acceptable for performing the mechanistic analyses that are the subject of this paper.

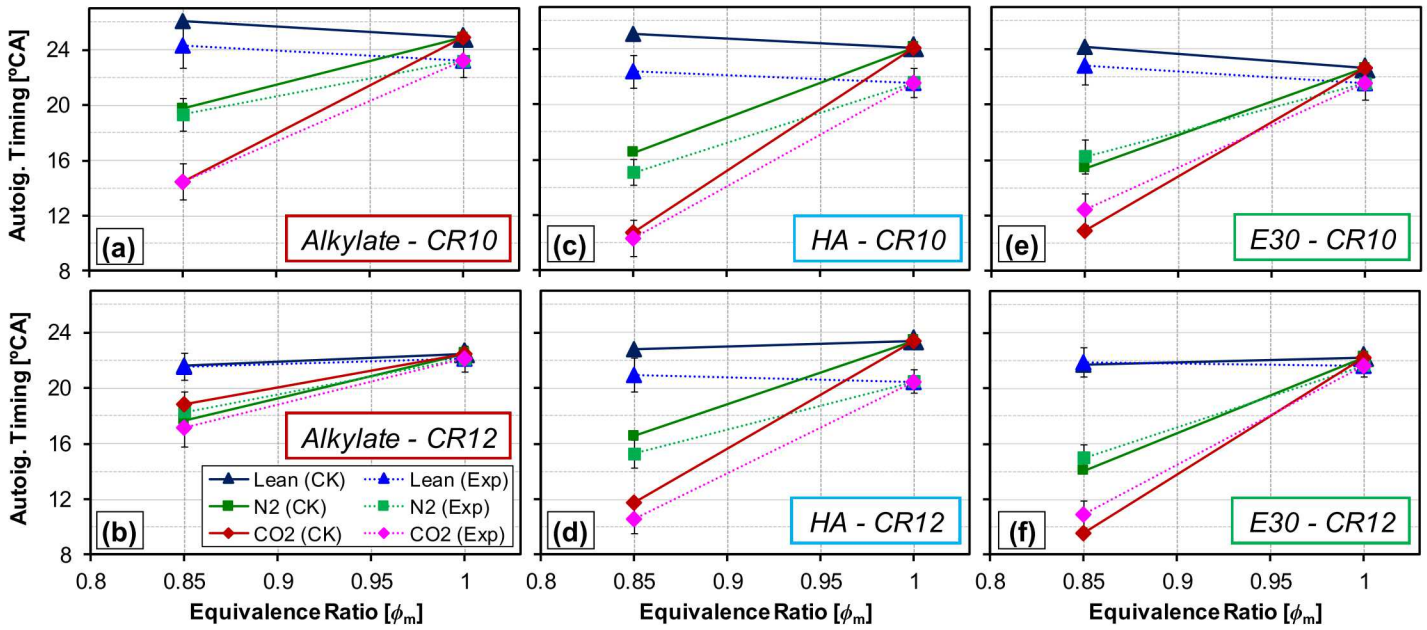

Figure 7. Comparison of measured and predicted autoignition timing at CR = 10 and 12, undiluted, with air dilution, N_2 dilution, and CO_2 dilution for Alkylate, High Aromatic, and E30.

Effect of fuel type on thermal stratification

Figure 8 presents the autoignition timings of simulations with varying initial temperatures for baseline conditions at CR = 10 without dilution. Here, the realizations consist of the adiabatic core (experimentally estimated temperature) as well as zones with 10 K steps in temperature reduction, in order to study the effect of thermal stratification on autoignition timing. To facilitate an interpretation of these results, the time between the experimentally measured autoignition timings and 90% burn point (CA90) are shown in Fig. 8 as well. The relevance of the CHEMKIN results presented here becomes more clear by comparing the time between measured autoignition timing and CA90, which is an approximation of the time available for deflagration to consume most of the end-gas mixture after autoignition in the adiabatic core occurs. In Fig. 8, it can be seen that for the High Aromatic and E30 fuels, the difference in autoignition timing of the hottest and the coldest zone is greater than 6.8°CA whereas for the Alkylate fuel, the difference is only 2.3°CA. Thus, the simulation result of the Alkylate fuel indicates that there is a higher probability of reactants in colder temperature zones to autoignite before deflagration reaches these cooler areas, while such phenomenon is less probable to happen for the other two fuels. Another interpretation of Fig. 8 is that the sequential autoignition in a thermally stratified end-gas volume has the potential to be very fast for Alkylate since the autoignition of the cooler zones is only marginally delayed by the cooler conditions. It is hypothesized that with a faster sequential autoignition, less autoigniting end-gas mass is sufficient to induce pressure oscillations, leading to acoustic knock. In Fig. 9, experimentally measured AHRRs are plotted against burned mass fraction with pink bars to indicate at which burned mass fraction the effect of autoignition becomes observable. Figure 9 shows that even though a smaller mass fraction autoignites for the Alkylate fuel compared to the E30 or High Aromatic fuels, the average KI is much higher for the Alkylate fuel. This experimental data presented in Fig. 9 supports the hypothesis of faster sequential autoignition being more prone to causing pressure oscillations in the cylinder.

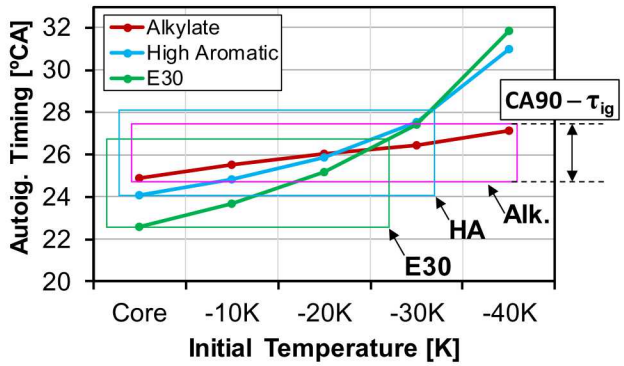

Figure 8. Autoignition timings in various temperature zones for the Alkylate, High Aromatic, and E30 fuels at CR = 10, undiluted condition. The time spent between autoignition timing to CA90 of corresponding cases is indicated by the height of the boxes.

Figure 10 presents simulated end-gas TP trajectories overlaid on constant-volume ignition delay maps for the baseline (undiluted) cases that corresponds to those shown in Fig. 8. The solid lines are trajectories of isentropic temperature and pressure. The isentropic temperatures were computed with the standard algebraic expression for the ideal isentropic relationship as shown in Equation 2, where T, P and γ are temperature, pressure, and condition-specific heat ratio, respectively.

$$T_{n+1} = T_n \left(\frac{P_{n+1}}{P_n}\right)^{(\gamma-1)/\gamma} \qquad (2)$$

To correctly compute the isentropic temperature, the specific heat ratio (γ) used in equation 2 should reflect both the gas composition and the temperature. In this study, γ was obtained conveniently from CHEMKIN with active chemistry, which strictly speaking is a deviation from isentropic conditions. The effect of this mismatch in γ on the computed isentropic temperature was estimated to be less than 5.5 K within the temperature regime studied here. In contrast, the dotted lines in Figure 10 show the temperature resulting from the combination of end-gas heat release and adiabatic compression. There are five sets of solid and dotted lines for each figures which correspond to the result obtained by successively reducing the initial temperatures at the start of the simulation in 10 K steps.

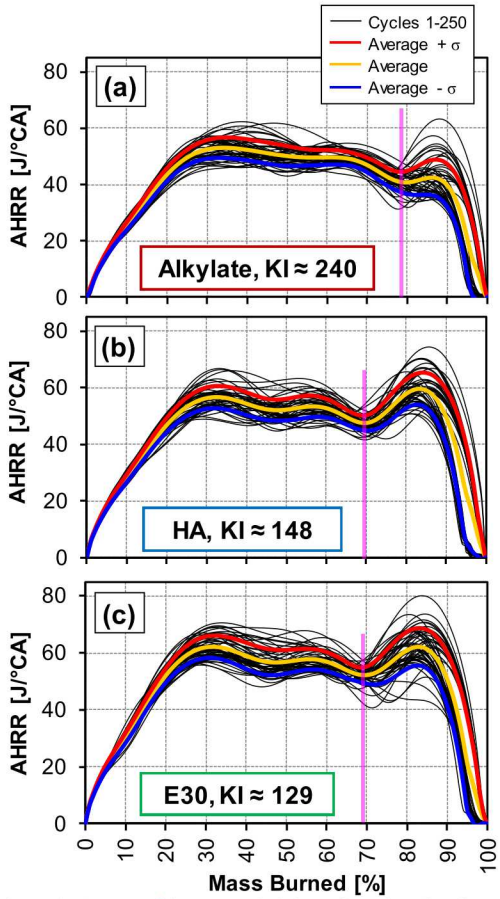

Figure 9. AHRR of downsampled data plotted against burned mass fraction for the Alkylate, High Aromatic, and E30 fuels at CR = 12, undiluted condition. The vertical lines in pink color indicate the burned mass fraction at the onset of the autoignition. Numbers in each plot indicate the average KI values of the downsampled dataset.

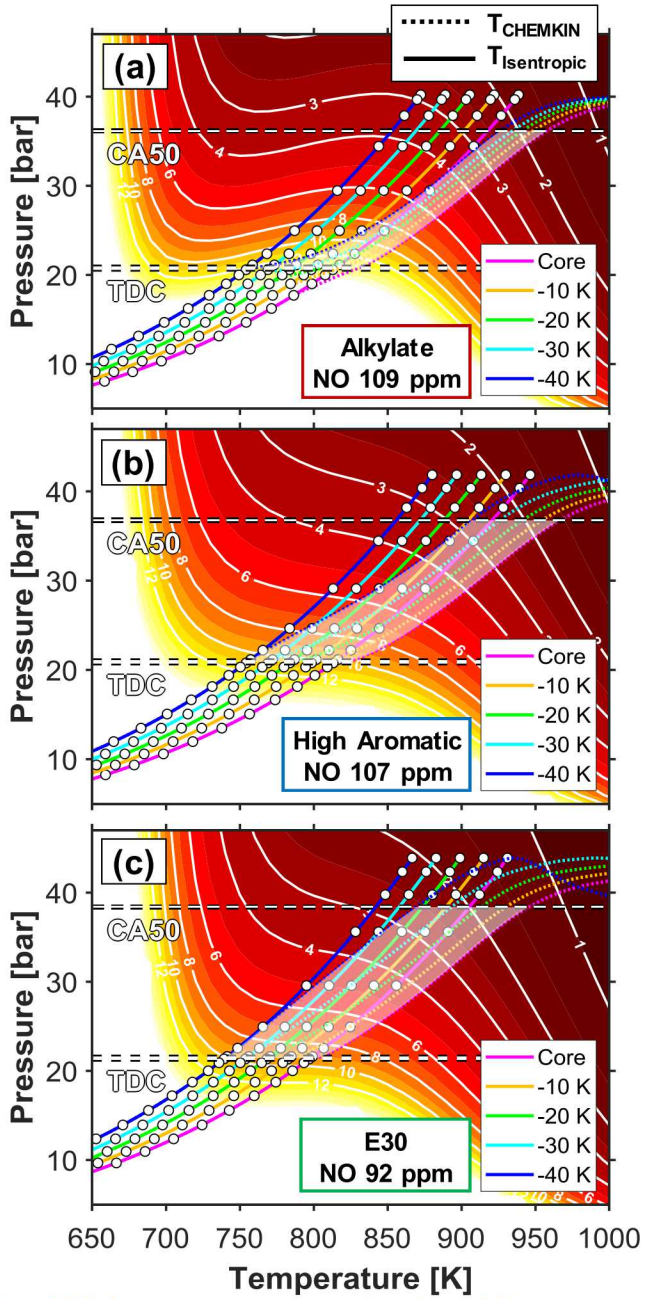

Figure 10. End-gas temperature-pressure trajectories overlaid on constant-volume ignition delay maps for undiluted stoichiometric charge, using the (a) Alkylate, (b) High Aromatic, and (c) E30 fuels at CR = 10. Solid lines represent end-gas temperature-pressure trajectories due to isentropic compression without chemical reactions; dashed lines represent end-gas temperature-pressure trajectories with chemical reactions and compression. Shaded regions highlight the change in thermal width with increasing pressure between TDC and CA50.

At a given pressure, the temperature difference between solid and dotted trajectories (with the same initial temperature) indicates the temperature rise due to chemical heat release until that point in time. The deviation at any point in time is not only dependent on the kinetic rates at a particular time step but also the residence time at each condition and the integrated effects of these various residence times. To illustrate the residence time that reactants spend in different regimes of the constant-volume ignition delay maps shown in Fig. 10, white circles are added on top of the solid isentropic trajectories. The time interval between adjacent circles is 0.5 ms in real time scale. If the circles are clustered, it indicates that the reactant in the end-gas is subjected to the given temperature and pressure for a longer period of time.

To clarify how the thermal stratification in the end-gas is altered by oxidation reactions under various conditions, a shaded area is added to highlight the evolution of thermal width between the temperatures of the hottest and the coldest zones. The shaded area continues from TDC up to the experimental CA50, which is when the change in thermal stratification is quantified for further analysis.

The temporal evolutions of thermal width shown in Fig. 10 are distinct from one fuel to the other. The thermal width of the Alkylate fuel shrinks significantly while that of the E30 fuel does not show a noticeable change. This is a consequence of a greater temperature rise in the coldest zone of the Alkylate fuel compared to the other zones, as shown in Fig. 11. With very similar residence time between TDC to CA50 for all three fuels, it is expected that the increased temperature rise in the coldest zone for Alkylate can be attributed to increased HRR.

To confirm and compare different characteristics of HRR in various temperature zones, HRR computed by CHEMKIN is shown in Fig. 12 for the three fuels. The figure indicates that low-temperature heat release (LTHR), indicated by its characteristic peak, dominates the autoignition chemistry prior to CA50. For all three fuels, the peak LTHR retards in phasing but increases in magnitude with a reduction of the initial temperature. However, the coldest zone of the Alkylate fuel exhibits much stronger LTHR than the other fuels, explaining the greater temperature rise in the coldest zone of the Alkylate fuel. The LTHR for the High Aromatic and E30 fuels in the hottest zone commences at similar timings (near -10°CA) while the peak magnitude LTHR for the E30 fuel is smaller and less distinct than that of the High Aromatic fuel. The peak magnitude of LTHR of the E30 fuel increases moderately with a reduction of the initial temperature. In the coldest zone of the E30 fuel, the location of peak LTHR is late and roughly coincides with CA50, which contributes to the small temperature rise plotted in Fig. 11. The smaller amount of LTHR of the E30 fuel results in reduced temperature rise in colder zones and helps to preserve the existing thermal stratification, as illustrated in Fig. 10(c). Weaker LTHR of the E30 fuel has been witnessed from previous experimental work with these fuels under similar conditions [28]. The low-HRR observed in the Core zone between the initial peak and the main ignition is indicative of Intermediate Temperature Heat Release (ITHR) as observed and discussed in [29] and [30].

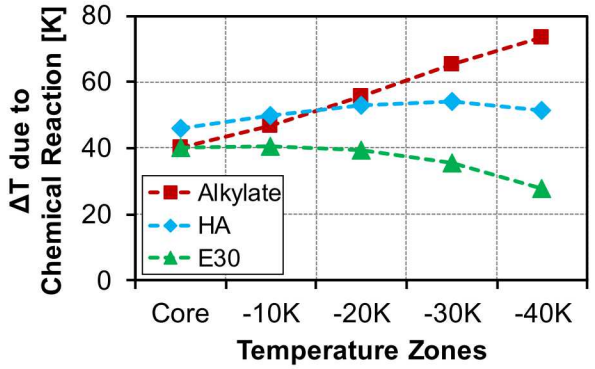

Figure 11. Comparison of temperature rise due to chemical reactions in various temperature zones at CA50 for CR = 10 and undiluted conditions.

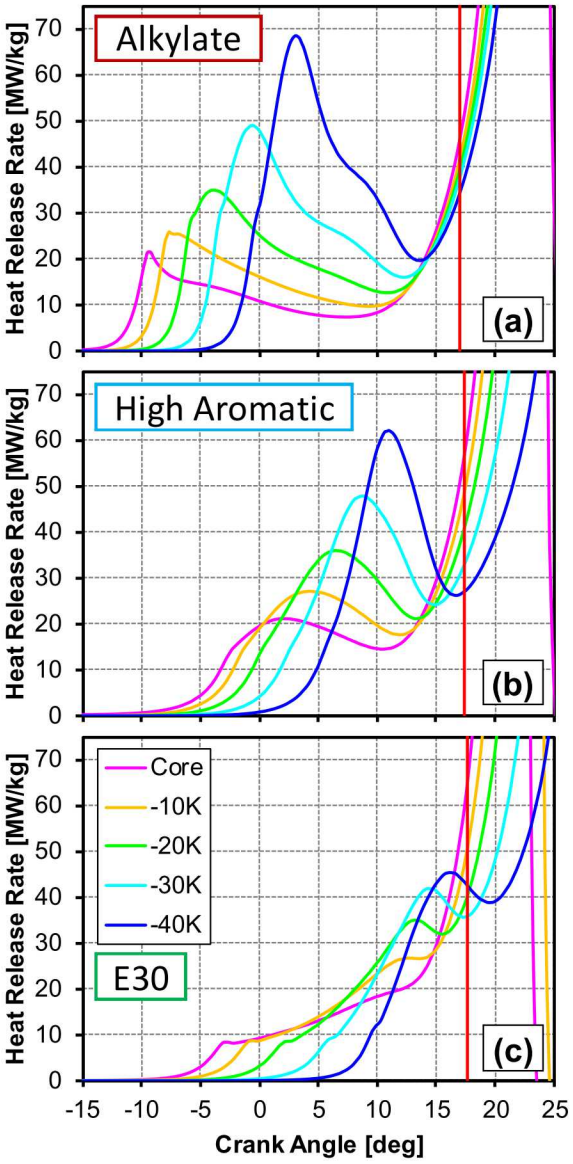

Figure 12. HRR in various temperature zones for the Alkylate, High Aromatic, and E30 fuels at CR10, undiluted condition. The red vertical line indicates location of CA50.

Effect of compression ratio on thermal stratification

Figure 13 plots mass fraction burned (MFB) at the onset of autoignition against CA50 for all diluted cases which share a common $\phi_m = 0.85$. Regardless of the fuel or CR, the general trend is that the MFB at the onset of autoignition increases with advancing CA50, meaning that the autoigniting mass fraction is reduced. This trend is consistent with HCCI research that showed that more thermal stratification is required to maintain acceptable ringing intensity as combustion phasing is advanced [31]. Comparing the two CRs at any given combination of fuel and CA50, it is observed that the CR = 12 case tolerates a larger autoigniting end-gas mass. In particular, Alkylate at CR = 10 tolerates very small fraction of autoigniting end-gas before knock becomes unacceptable. It is hypothesized that for the higher CR, heat transfer in the end-gas region is stronger and enhances the thermal stratification, which acts to smooth sequential autoignition [31] and mitigate the occurence of acoustic knock. This hypothesis is supported by a comparison of the squish heights shown in Fig. 1 (a) and (b). For the higher CR, the squish height at the edge of the piston is reduced by 30% from 6.8 mm to 4.8 mm. With shorter distances for diffusive and convective heat transfer, the gas located in the squish region is expected to undergo increased interaction with the thermal boundary layer near the wall. The hypothesis of increased heat transfer and enhanced thermal stratification at the higher CR is also supported by the observed difference in the gross indicated mean effective pressure (gIMEP) of motored condition from two CRs. The measured gIMEP at CR = 10 and 12 were -37.9 kPa and -51.0 kPa, respectively. This result suggests that the heat transfer loss at CR = 12 increases by roughly 35%, based on the assumption that the differences in the gIMEP is attributable solely to the heat transfer and blow-by is not significantly different at two CRs.

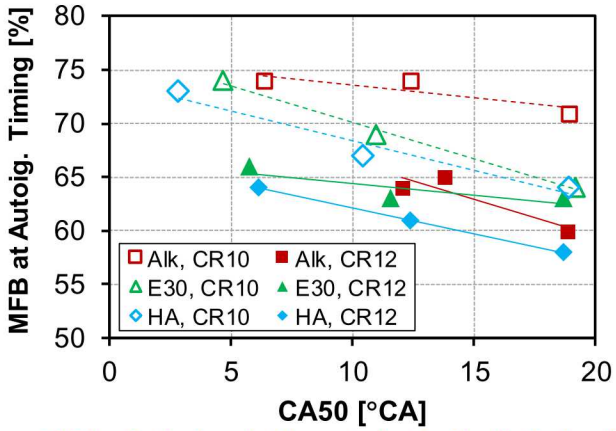

Figure 13. Mass fraction burned at the onset of autoignition for the three fuels with dilution. The linear fits are obtained for the downsampled dataset of 50 cycles that corresponds to each combination of the fuel and CR.

Besides the likelihood of an enhanced thermal stratification for the higher CR, the effects of chemistry in the various temperature zones were observed to exhibit significant differences as well. Figure 14 shows a comparison of the temperature rise due to chemical reactions in various temperature zones and the experimentally determined KL-CA50 for the CO_2-diluted conditions. As explained in [18], the combination of the Alkylate fuel and CR = 12 leads to increased temperature rise due to chemical reactions in lower temperature zones which reduces the thermal stratification, here indicated by the steeper positive slope in Fig. 14(a).

The temperature rise due to chemical reactions in the end-gas of High Aromatic – oxidizer mixtures is relatively uniform across temperature zones. Increasing CR from 10:1 to 12:1 affects the end-gas heat release, resulting in greater temperature rise, especially in the lowest temperature zones. However, the magnitude and variance in end-gas temperature rise is low when compared to that predicted for the Alkylate fuel. Therefore, the effect of heat release on thermal stratification is small in this case, due to the uniformity of the heat release, in contrast to the Alkylate fuel at CR = 12.

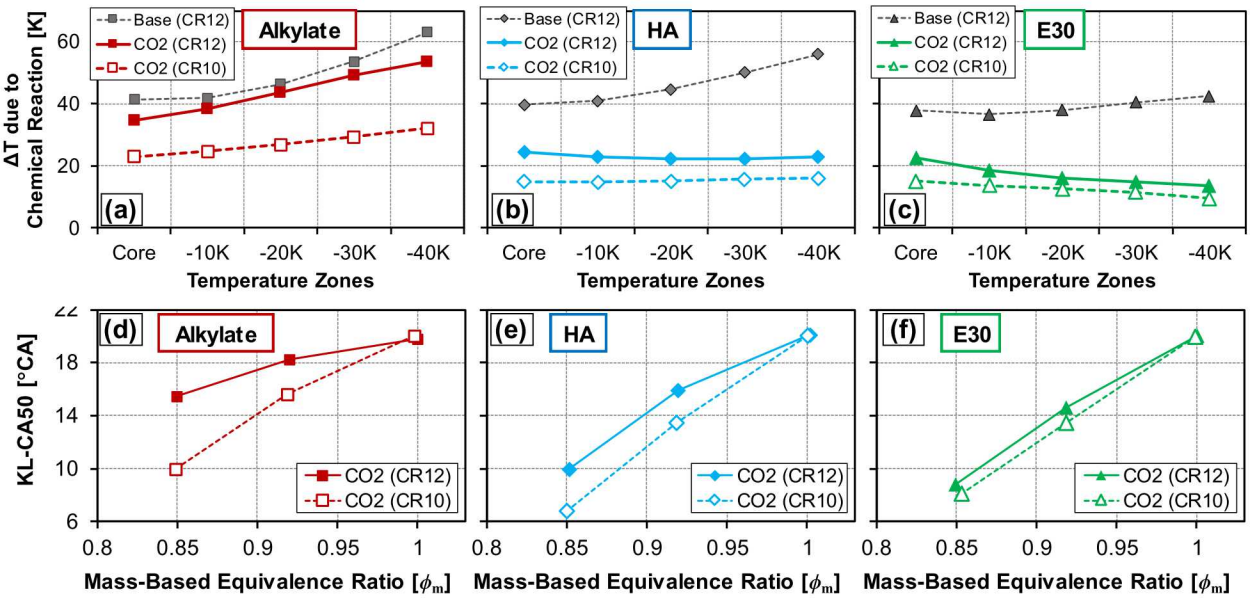

Figure 14. Comparison of temperature rise due to chemical reaction to experimentally measured KL-CA50 for CO_2-diluted condition. CO_2 cases in (a) – (c) all have $\phi_m = 0.85$.

The E30 fuel exhibits the lowest magnitude of temperature rise in the end-gas due to heat release, with 8 K being the maximum difference across the simulated conditions for CR = 10 and 12, which is even smaller than that observed for High Aromatic fuel (~10 K), and much smaller than that observed for the Alkylate fuel (~22 K). For either CR, the slope is slightly negative in Fig. 14(c), which works to enhance thermal stratification for the E30 fuel, regardless of CR.

Figure 15 shows the autoignition timings in various temperature zones for the CO_2-diluted condition with all three fuels. To indicate the effect of thermal stratification on sequential autoignition, the sensitivity of individual-zone autoignition timings to the initial temperature was obtained using linear regressions. For the linear fit, the autoignition timings in the coldest zones were excluded. This was done for a more fair comparison because for the Alkylate fuel, the sensitivity of autoignition timing for the coldest zone deviates significantly from linearity. The slope of the linear fit and differences in the slopes of two CRs agree well with the characteristics of temperature rise due to chemical reactions shown in Fig. 14. This confirms that maintaining thermal stratification despite ongoing early autoignition reactions is important for achieving sequential autoignition. However, the sequential autoignition itself is not sufficient to explain some of the differences in KL-CA50 of different fuels. For example, the Alkylate fuel at CR = 10 shows the steepest slope in the autoignition timing of various temperature zones, suggesting that autoignition should occur more sequentially. However, the KL-CA50 that corresponds to this case is not the most advanced CA50 compared to other cases. This suggests that the sequential autoignition is not the only important factor for suppressing knock, but also a reduction in the overall temperature rise due to chemical reaction.

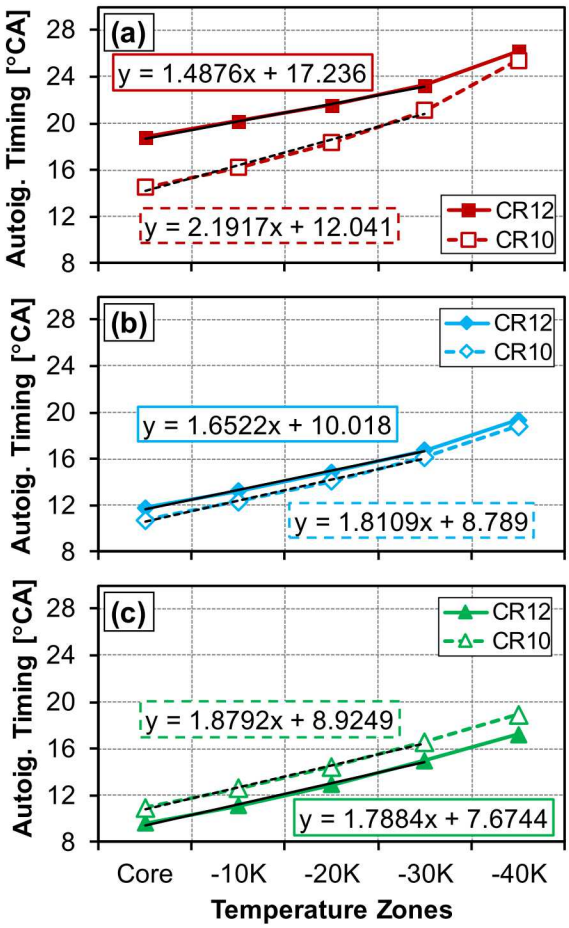

Figure 15. Autoignition timings in various temperature zones for the (a) Alkylate, (b) High Aromatic, and (c) E30 fuels at CR = 10 and 12, CO_2-diluted condition with $\phi_m = 0.85$. The linear fits exclude the coldest zone of each case. The equations of linear regressions for the two CRs are identified by the border of the box: dashed line for CR = 10 and solid line for CR = 12.

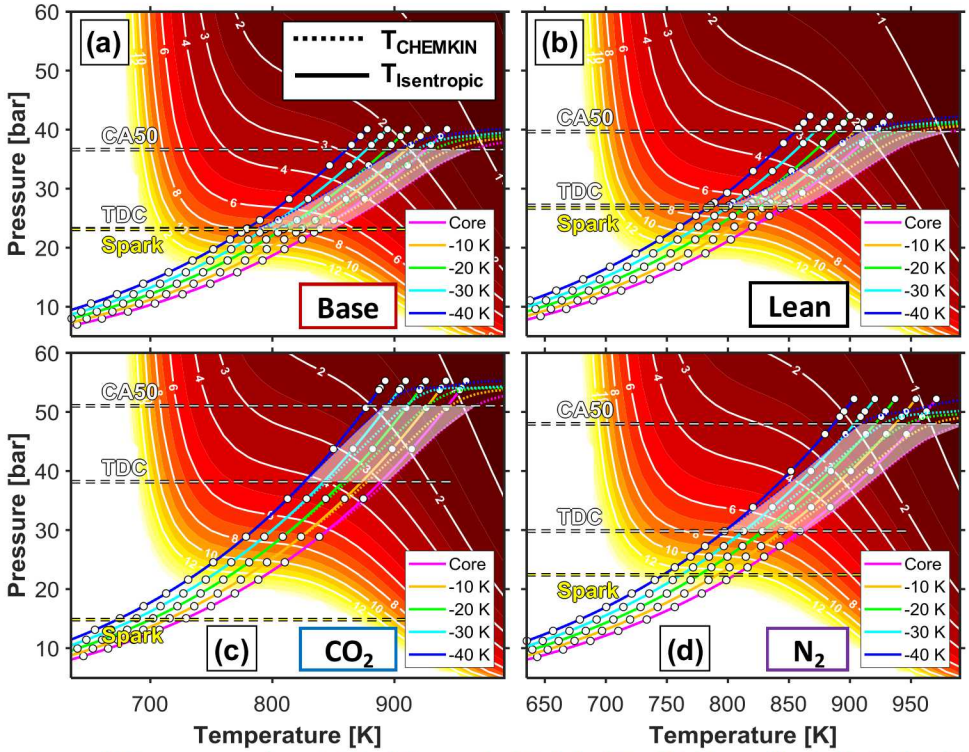

Figure 16. End-gas TP trajectories overlaid on constant-volume ignition delay map for E30 fuel at CR = 12, (a) non-diluted, (b) air-diluted, (c) CO_2-diluted, and (d) N_2-diluted conditions. All diluted cases have $\phi_m = 0.85$. Solid lines represent end-gas temperature-pressure trajectories due to isentropic compression without chemical reactions; dashed lines represent end-gas temperature-pressure trajectories with chemical reactions and compression.

Effect of diluent types on thermal stratification - E30, CR12

Figure 16 shows the end-gas TP trajectories overlaid on constant-volume ignition delay maps for the E30 fuel at both undiluted and diluted conditions for CR = 12. At the peak pressure and temperature of the isentropic TP trajectories, the corresponding ignition delay of the end-gas is in the 0.8-1.5 ms range for the hottest core zone, depending on the diluent. The constant-volume ignition delay maps shown in the background of Fig. 16 show that when N_2 or CO_2 is added, the contours of the constant-volume ignition delay are shifted, indicating that the reactants become less reactive for a given initial temperature and pressure. This can be attributed to a reduction of both fuel and oxygen concentrations. The smaller shift in ignition delay contours for the air-diluted (lean) condition is attributable to a slight increase of NO as indicated in Table 5, which partly compensates for the reduction of fuel concentration.

Figure 16 also allows a comparison of differences in the evolution of thermal width, as illustrated by differences in the shaded regions. The thermal width of the CO_2-diluted case exhibits the smallest change when phasing spans from TDC to CA50. This occurs because the amount of temperature rise associated with autoignition reactions is small for all temperature zones, resulting in small deviations between the isentropic temperature and the temperature of the reacting charge. Both a shorter residence time and a reduced reactivity contribute to lower the amount of temperature rise associated with autoignition reactions. The advanced combustion phasing shortens residence time between TDC to CA50, as illustrated by very few 0.5 ms-indicating circles, which reduces time for accumulation of heat from chemical reactions. Contributing to a reduced reactivity are reduced compressed temperatures due to a lower γ, as well as a reduction of the oxygen mole fraction. Hence, the combined effects of a lower reactivity and faster traverse through TP space compound to allow a strong advancements of CA50 for operation with CO_2 dilution.

Figure 17 summarizes the complex interaction between different magnitudes of LTHR and residence times shown in Fig. 16. The negative slope for both the CO_2- and N_2-diluted cases shows that a broadening of the thermal width takes place, unlike the undiluted base condition. The CO_2 and N_2 cases both beneficially reduce the overall temperature rise due to chemical reactions, consistent with the knock-suppression effects of these diluents (*cf.* Fig. 7(f)). In contrast, the positive slopes of the base and lean cases in Fig. 17 show that a slight narrowing of the thermal width occurs for these two cases. Furthermore, the lean case exhibits higher overall temperature rise due to chemical reactions compared to the base case, and this is consistent with its inability to provide any knock suppression (*cf.* Fig. 7(f)).

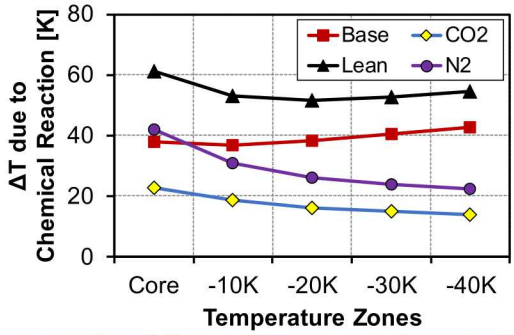

Figure 17. Effect of diluents on temperature rise due to chemical reactions in the end-gas for E30 fuel at CR = 12, corresponding to Fig. 16. All diluted cases have $\phi_m = 0.85$.

Summary of simulation results

To summarize these modeling results, the degree of sequential autoignition is compared with how the engine has to be operated relative to trace-autoignition conditions to avoid excessive knock. Trace Autoignition CA50 is the most retarded combustion phasing for which the effect of autoignition can be observed on the experimental HRR. The methodology for determining the Trace Autoignition CA50 can be found in Fig. A2 in Appendix A. The crank-angle span from Trace Autoignition CA50 to the actual average KL-CA50 is a metric that indicates how far CA50 can be advanced without incurring strong knock relative to CA50 at which end-gas autoignition starts to occur. Figure 18 shows a reasonable correlation between these metrics, which supports the general hypothesis that thermal stratification and sequential autoignition are important for the knock performance of the engine. Generally, Fig. 18 shows that when the model indicates a more sequential autoignition for a given amount of thermal stratification, the experimental data show that it is possible to operate the engine with a KL-CA50 that is further advanced beyond the Trace Autoignition CA50.

As discussed in the previous section, the sequential autoignition itself is not sufficient to explain the effectiveness of a diluent for knock suppression (quantified from the KL-CA50 advancement relative to the baseline condition). To better understand the effectiveness of each diluent, it is necessary to observe how each diluent affects autoignition reactions in the end gas, and associated heat release and temperature rise. Figure 19 compares the effects of diluents on end-gas heat release and temperature rise by comparing diluted cases to their baseline conditions, and how this corresponds to the change in Trace Autoignition CA50. The average increase in temperature due to chemical reactions was obtained by computing the average of temperature rise from all five temperature zones. Dilution with air results in a greater temperature increase in the end-gas compared to the baseline condition, whereas dilution with CO_2 significantly reduces the temperature rise in the end-gas. This explains why the timing for the onset of autoignition could not be advanced when air was used as a diluent. A strong correlation between Trace Autoignition CA50 and the average temperature increase in the end-gas confirms that the temperature is the key parameter that triggers autoignition.

Thus, for a diluent to be effective in suppressing knock and enable more advanced KL-CA50, it is necessary to achieve a reduction in the end-gas temperature to achieve a more advanced Trace Autoignition CA50. Such temperature reduction can be accomplished by reducing the amount of chemical reactions and by lowering compression heating (via reduced γ and lower ϕ_m). Further advancement of KL-CA50 can be accomplished by inducing a more sequential autoignition in the end-gas to enable the combustion phasing to be advanced relative to Trace Autoignition CA50 without incurring acoustic knock.

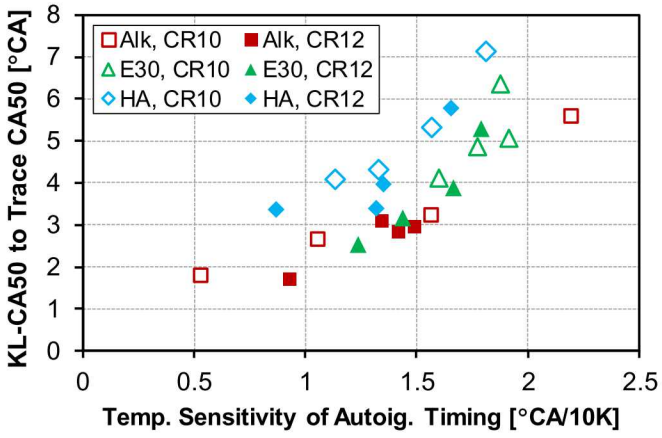

Figure 18. Comparison of experimentally measured advancement of KL-CA50 relative to trace autoignition with simulated temperature sensitivity of the end-gas autoignition timing (following analysis shown in Fig. 15).

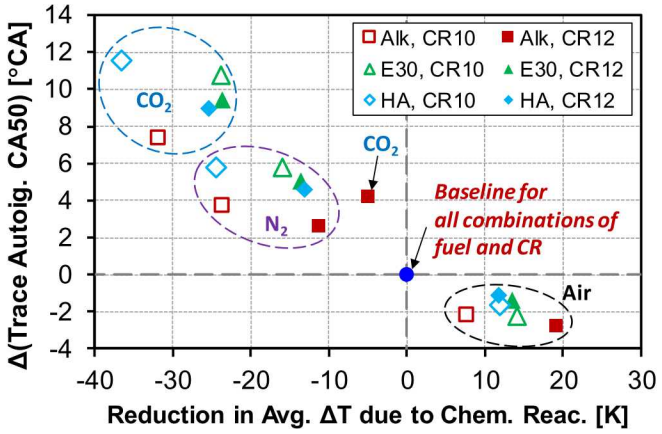

Figure 19. Comparison of reduction in average of temperature rise in various temperature zones and advancement of Trace Autoignition CA50 with diluent addition.

Implication of Sequential Autoignition on Knock Intensity Distribution

To illustrate the effect of sequential autoignition in the end-gas on the resulting pressure oscillations (here quantified as knock intensity), distributions of KI plotted against CA50 are compared for the Alkylate and E30 fuels at CR = 12, undiluted conditions. These conditions were chosen to minimize any bias that could be caused by difference in the average CA50 and cycle-to-cycle variation in CA50. Although the selected conditions have nearly identical average KI, CA50 and cycle-to-cycle variation of CA50, Fig. 20 presents very distinct KI distributions for the two cases. For the Alkylate fuel, a steep rise in KI value can be observed when CA50 is advanced beyond Trace Autoignition CA50. On the other hand, a more gradual increase in KI values with advanced CA50 can be seen for the E30 fuel. The number of cycles with combustion phasing advanced beyond the trace autoignition phasing for the E30 fuel is greater than 60% of the total numbers of cycles in the dataset. In contrast, the Alkylate only has ~35% of cycles with CA50 advanced beyond trace autoignition. Corresponding modeling results of the autoignition

timings in various temperature zones are shown in Fig. 21. Autoignition in lower temperature zones occur more sequentially for the E30 fuel compared to the Alkylate fuel. The comparison of Figs. 20 and 21 lends further supports to the general hypothesis that sequential autoignition due to thermal stratification helps to mitigate acoustic knock of autoigniting cycles.

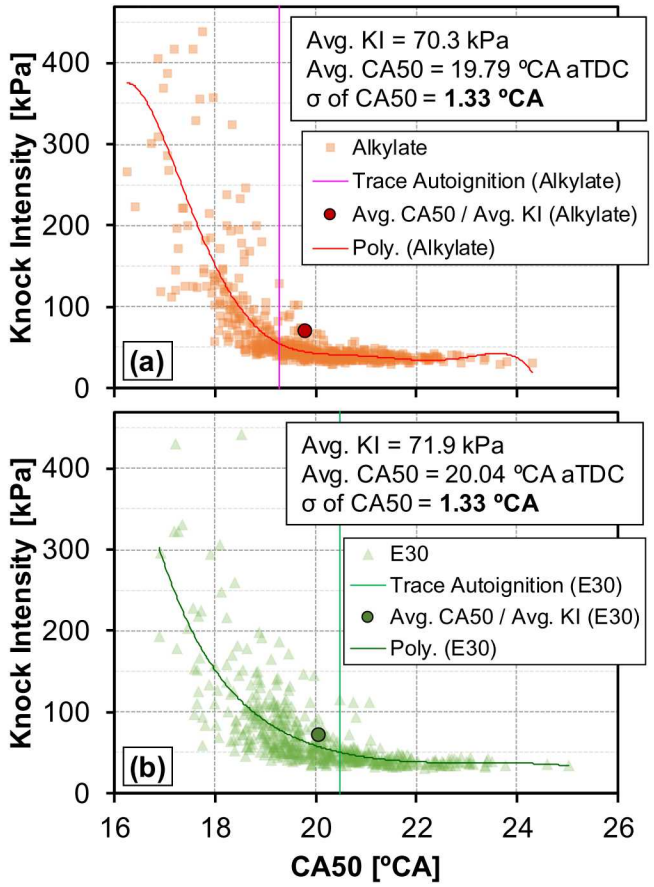

Figure 20. Distribution of single-cycle KI values plotted against CA50 for the Alkylate and E30 fuels at CR = 12, undiluted baseline condition.

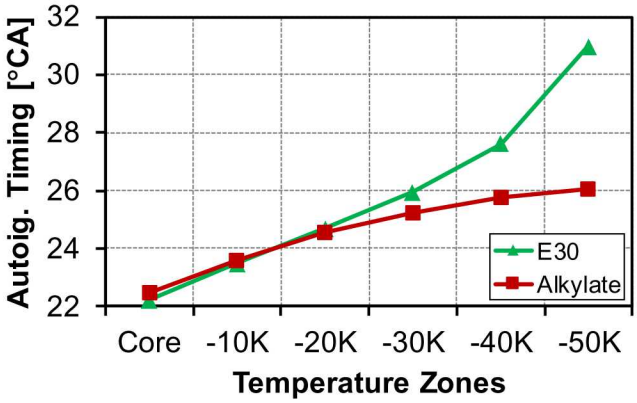

Figure 21. Autoignition timings in the various temperature zones for the Alkylate and E30 fuels at CR = 12, undiluted baseline condition.

Summary and Conclusions

SI-engine experiments showed that the efficacy of N_2 and CO_2 to suppress knock varies greatly with fuel type and compression ratio (CR). To clarify the factors that govern these different responses to EGR constituents, the end-gas autoignition processes were studied numerically using a detailed chemical-kinetic description. The analysis included the effects of varying temperature-pressure trajectories, diluents, fuels, and thermal stratification. The ability of end-gas thermal stratification to create a sequential autoignition event and reduce the risk of acoustic knock was a guiding hypothesis in this study, and the experimental and modeling results were found to be consistent with this hypothesis.

The results demonstrate that fuels with a matched RON = 98 can exhibit strong variations in behavior at both diluted and undiluted conditions. General observations are:

Early autoignition heat release in the end-gas, *i.e.* between TDC and 50% burn point (CA50), that precedes hot ignition and thermal run-away tends to be dominated by low-temperature heat release (LTHR). This is particularly true for the Alkylate fuel whose composition is dominated by alkanes, and characterized by its low RON-MON octane sensitivity (S) of 1.

In addition to the Alkylate fuel's oxidization chemistry and reactant composition, the magnitude of the LTHR depends on the amount of time spent in the 750 – 900K temperature range. Hence, the LTHR varies with CR, CA50, and thermal stratification caused by heat transfer to the combustion-chamber walls. Changes to the engine operation that reduce the LTHR magnitude and associated temperature rise also suppress knock, contributing to enable a beneficial advancement of CA50.

Due to the inherent Negative Temperature Coefficient (NTC) character of the Alkylate fuel's autoignition, its LTHR becomes stronger in regions that are cooler than the adiabatic core, and this counteracts a given thermal stratification, effectively making the end-gas more thermally uniform. When this occurs, the sequential autoignition and transition into hot ignition happens faster, forcing the use of a more retarded CA50 to avoid engine knock. The High-Aromatic and E30 fuels do not have an inherent NTC character, but ignition delay maps reveal temperature-pressure regions with very low temperature sensitivity of autoignition. Hence, there are conditions even for these high-S fuels, particularly without EGR dilution, where LTHR counteracts a given thermal stratification. Generally, conditions with low LTHR and a preserved thermal stratification allow an advanced CA50 relative to the CA50 where trace autoignition occurs, contributing to advance the knock-limited combustion phasing (KL-CA50).

Increased CR allows a larger autoigniting end-gas mass fraction for a given KL-CA50. It is speculated that the smaller squish height at CR = 12 increases the heat transfer from the end-gas to the wall, which broadens the thermal width and promotes a sequential autoignition event with reduced peak HRR.

Overall, for the conditions covered here, the knock responses to changes of EGR diluents and CR for the two high-S fuels are fairly similar despite large differences in composition and substantial differences in LTHR magnitudes. If this similarity holds for other operating conditions, RON and MON may provide sufficient specificity to the fuel properties of future gasoline fuels that are

designed to promote the implementation of SI engines that utilize high EGR rates in the quest for higher efficiency.

References

1. Alger, T., Gingrich, J., Roberts, C., and Mangold, B., "Cooled exhaust-gas recirculation for fuel economy and emissions improvement in gasoline engines," *Int. J. Engine Res*. 12(3):252-264, 2011, doi:10.1177/1468087411402442.
2. Takaki, D., Tsuchida, H., Kobara, T., Akagi, M. et al., "Study of an EGR System for Downsizing Turbocharged Gasoline Engine to Improve Fuel Economy," SAE Technical Paper 2014-01-1199, 2014, doi:10.4271/2014-01-1199.
3. Hwang, K., Hwang, I., Lee, H., Park, H. et al., "Development of New High-Efficiency Kappa 1.6L GDI Engine," SAE Technical Paper 2016-01-0667, 2016, doi:10.4271/2016-01-0667.
4. Matsuo, S., Ikeda, E., Ito, Y., and Nishiura, H., "The New Toyota Inline 4 Cylinder 1.8L ESTEC 2ZR-FXE Gasoline Engine for Hybrid Car," SAE Technical Paper 2016-01-0684, 2016, doi:10.4271/2016-01-0684.
5. Grandin, B. and Ångström, H., "Replacing Fuel Enrichment in a Turbo Charged SI Engine: Lean Burn or Cooled EGR," SAE Technical Paper 1999-01-3505, 1999, doi:10.4271/1999-01-3505.
6. Siokos, K., Koli, R., Prucka, R., Schwanke, J. , "Assessment of Cooled Low Pressure EGR in a Turbocharged Direct Injection Gasoline Engine," *SAE Int. J. Engines* 8(4):1535–1543, 2015, doi:10.4271/2015-01-1253.
7. Kumano, K. and Yamaoka, S., "Analysis of Knocking Suppression Effect of Cooled EGR in Turbo-Charged Gasoline Engine," SAE Technical Paper 2014-01-1217, 2014, doi:10.4271/2014-01-1217.
8. Szybist, J., Wagnon, S., Splitter, D., Pitz, W. et al., "The Reduced Effectiveness of EGR to Mitigate Knock at High Loads in Boosted SI Engines," *SAE Int. J. Engines* 10(5):2017, doi:10.4271/2017-24-0061.
9. Splitter, Derek A., and James P. Szybist. "Experimental investigation of spark-ignited combustion with high-octane biofuels and EGR. 1. Engine Load Range and Downsize Downspeed Opportunity," *Energ. Fuels* 28(2):1418–1431, 2014, doi:10.1021/ef401574p.
10. Splitter, Derek A., and James P. Szybist. "Experimental investigation of spark-ignited combustion with high-octane biofuels and EGR. 2. Fuel and EGR effects on knock-limited load and speed," *Energ. Fuels* 28(2):1432-1445, 2014, doi:10.1021/ef401575e.
11. Sjöberg, M., Dec, J., and Hwang, W., "Thermodynamic and Chemical Effects of EGR and Its Constituents on HCCI Autoignition," SAE Technical Paper 2007-01-0207, 2007, doi:10.4271/2007-01-0207.
12. Francqueville, L. and Michel, J., "On the Effects of EGR on Spark-Ignited Gasoline Combustion at High Load," *SAE Int. J. Engines* 7(4):1808-1823, 2014, doi:10.4271/2014-01-2628.
13. Hoppe, F., Thewes, M., Baumgarten, H., and Dohmen, J., "Water injection for gasoline engines: Potentials, challenges, and solutions," *Int. J. Engine Res.* 17(1):86-96, 2016, doi:10.1177/1468087415599867.
14. Kim, J., Park, H., Bae, C., Choi, M. et al., "Effects of water direct injection on the torque enhancement and fuel consumption reduction of a gasoline engine under high-load conditions," *Int. J. Engine Res.* 17(7):795-808, 2016, doi:10.1177/1468087415613221.
15. Kawabata, Y., Sakonji, T., and Amano, T., "The Effect of NOx on Knock in Spark-ignition Engines," SAE Technical Paper 1999-01-0572, 1999, doi:10.4271/1999-01-0572.
16. Stenlåås, O., Einewall, P., Egnell, R., and Johansson, B., "Measurement of Knock and Ion Current in a Spark Ignition Engine with and without NO Addition to the Intake Air," SAE Technical Paper 2003-01-0639, 2003, doi:10.4271/2003-01-0639.
17. Roberts, P. and Sheppard, C., "The Influence of Residual Gas NO Content on Knock Onset of Iso-Octane, PRF, TRF and ULG Mixtures in SI Engines," *SAE Int. J. Engines* 6(4):2028-2043, 2013, doi:10.4271/2013-01-9046.
18. Vuilleumier, D., Kim, N., Sjöberg, M., Yokoo, N. et al., "Effects of EGR Constituents and Fuel Composition on DISI Engine Knock: An Experimental and Modeling Study," SAE Technical Paper 2018-01-1677, 2018, doi:10.4271/2018-01-1677.
19. ANSYS CHEMKIN-PRO 18.1, ANSYS: San Diego, 2017.
20. Sjöberg, M., Vuilleumier, D., Yokoo, N., and Nakata, K., "Effects of Gasoline Composition and Octane Sensitivity on the Response of DISI Engine Knock to Variations of Fuel-Air Equivalence Ratio," The International Symposium on Diagnostics and Modeling of Combustion in Internal Combustion Engines, 2017(9):B307, 2017, doi:10.1299/jmsesdm.2017.9.B307.
21. Petitpas, G., McNenly, M., and Whitesides, R., "A Framework for Quantifying Measurement Uncertainties and Uncertainty Propagation in HCCI/LTGC Engine Experiments," *SAE Int. J. Engines* 10(3):1275-1296, 2017, doi:10.4271/2017-01-0736.
22. Sjöberg, M., Dec, J., Babajimopoulos, A., and Assanis, D., "Comparing Enhanced Natural Thermal Stratification Against Retarded Combustion Phasing for Smoothing of HCCI Heat-Release Rates," SAE Technical Paper 2004-01-2994, 2004, doi:10.4271/2004-01-2994.
23. Netzer, C., Seidel, L., Pasternak, M., Lehtiniemi, M. et al., "Three-dimensional computational fluid dynamics engine knock prediction and evaluation based on detailed chemistry and detonation theory," *Int. J. of Engine Res.* 19(1):33-44, 2017, doi:10.1177/1468087417740271.
24. Dronniou, N. and Dec, J., "Investigating the Development of Thermal Stratification from the Near-Wall Regions to the Bulk-Gas in an HCCI Engine with Planar Imaging Thermometry," *SAE Int. J. Engines* 5(3):1046-1074, 2012, doi:10.4271/2012-01-1111.
25. Sjöberg, M., Dec, J., and Cernansky, N., "Potential of Thermal Stratification and Combustion Retard for Reducing Pressure-Rise Rates in HCCI Engines, Based on Multi-Zone Modeling and Experiments," SAE Technical Paper 2005-01-0113, 2005, doi:10.4271/2005-01-0113.
26. Mehl, M., Chen, J., Pitz, W., Sarathy, S. et al., "An approach for formulating surrogates for gasoline with application toward a reduced surrogate mechanism for CFD engine modeling," *Energ. Fuels* 25(11):5215-5223, 2011, doi:10.1021/ef201099y.
27. Sjöberg, M. and Dec, J., "An Investigation of the Relationship Between Measured Intake Temperature, BDC Temperature, and Combustion Phasing for Premixed and DI HCCI Engines," SAE Technical Paper 2004-01-1900, 2004, doi:10.4271/2004-01-1900.

28. Vuilleumier, D. and Sjöberg, M., "Significance of RON, MON, and LTHR for Knock Limits of Compositionally Dissimilar Gasoline Fuels in a DISI Engine," *SAE Int. J. Engines* 10(3):938-950, 2017, doi:10.4271/2017-01-0662.
29. Mehl, M., Pitz, W., Sarathy, M., Yang, Y. et al., "Detailed Kinetic Modeling of Conventional Gasoline at Highly Boosted Conditions and the Associated Intermediate Temperature Heat Release," SAE Technical Paper 2012-01-1109, 2012, doi:10.4271/2012-01-1109.
30. Vuilleumier, D., Kozarac, D., Mehl, M., Saxena, S. et al, "Intermediate temperature heat release in an HCCI engine fueled by ethanol/n-heptane mixtures: An experimental and modeling study," Combust Flame. 161(3): 680-695, 2014, doi:10.1016/j.combustflame.2013.10.008.
31. Sjöberg, M. and Dec, J., "Effects of Engine Speed, Fueling Rate, and Combustion Phasing on the Thermal Stratification Required to Limit HCCI Knocking Intensity," SAE Technical Paper 2005-01-2125, 2005, doi:10.4271/2005-01-2125.
32. Heywood, J., *Internal Combustion Engine Fundamentals* (New York: McGraw-Hill, 1988).
33. Borg, J. and Alkidas, A., "Characterization of Autoignition in a Knocking SI Engine Using Heat Release Analysis," SAE Technical Paper 2006-01-3341, 2006, doi:10.4271/2006-01-3341.

Acknowledgments

The authors would like to thank Alberto Garcia, Gary Hubbard, Keith Penney, Chris Carlen and Tim Gilbertson for their dedicated support of the DISI laboratory. Dario Lopez-Pintor and Gerald Gentz provided valuable feedback on the manuscript.

Financial support for this study was provided by Toyota Motor Corporation under agreement FI 083130924. Support for establishing the engine lab used in this study was provided by the Vehicle Technologies Office at U.S. Department of Energy (DOE), Office of Energy Efficiency and Renewable Energy (EERE). The fuels used in this study were developed as part of the Co-Optimization of Fuels & Engines (Co-Optima) project sponsored by the U.S. DOE. Sandia National Laboratories is a multimission laboratory managed and operated by National Technology and Engineering Solutions of Sandia, LLC., a wholly owned subsidiary of Honeywell International, Inc., for the U.S. Department of Energy's National Nuclear Security Administration under contract DE-NA0003525. Delphi Technology is gratefully acknowledged for providing the Delphi Multec® 3.5HT port fuel injector, which was used for injecting distilled water into the intake system.

Definitions/Abbreviations

AHRR	Apparent Heat Release Rate
AKI	Anti-Knock Index
aTDC	after Top Dead Center
°CA	Degrees Crank Angle
CA50	50% Burn Point
CA90	90% Burn Point
CO_2	Carbon Dioxide
CO	Carbon Monoxide
Co-Optima	Co-Optimization of Fuels and Engines
CR	Compression Ratio
DISI	Directly-Injected Spark Ignition
EGR	Exhaust Gas Recirculation
γ	Specific Heat Ratio
gIMEP	Gross Indicated Mean Effective Pressure
H_2	Hydrogen
H_2O	Water
HoV	Heat of Vaporization
HRR	Heat Release Rate
ITHR	Intermediate Temperature Heat Release
K	Kelvin
KI	Knock Intensity
KL-CA50	Knock-Limited Combustion Phasing
LTHR	Low-Temperature Heat Release
MFB	Mass fraction burned
MON	Motor Octane Number
ms	milliseconds
N_2	Nitrogen
NO	Nitric Oxide
NO_2	Nitrogen Dioxide
NTC	Negative Temperature Coefficient
OH	Hydroxyl radical
ϕ_m	Charge-mass based equivalence ratio

ϕ	Equivalence ratio	**TDC**	Top Dead Center
RON	Research Octane Number	**UHC**	Unburned hydrocarbon
S	Octane Sensitivity		
SI	Spark Ignition		

Appendix A: Experimental procedures and definitions of Knock Intensity and Trace Autoignition

For each operating point, the engine was allowed to run for several minutes until all measured parameters were stable, especially knock intensity, at which point measurements were recorded. The in-cylinder pressure, spark current, intake and exhaust pressure, and fuel pressure were acquired for 500 consecutive cycles using 0.1 degrees crank-angle (°CA) resolution. In-cylinder pressure was measured using an uncooled Kistler 6125C piezoelectric sensor in combination with a Kistler 5010B charge amplifier. The crank angle is defined as zero at TDC combustion, therefore given as negative numbers during the intake and compression strokes.

The apparent heat-release rate (AHRR) was computed from the in-cylinder pressure for each individual cycle using a constant ratio of specific heats ($\gamma = 1.33$) following [32]. For computing combustion-phasing metrics like the 50% burn point (CA50), the AHRR was integrated from the spark timing to the crank-angle where AHRR drops to zero again, then scaled so that it rises from 0 to 100% for every cycle, irrespective of the actual combustion efficiency (which was greater than 95.7% for all cases).

The KI metric was calculated from measured cylinder pressure, which was processed on a cycle-by-cycle basis over several steps. The measured pressure trace was first low-pass filtered (<1.5 kHz) and subtracted from the unfiltered trace. Using Fourier decomposition, the energy content in the 0 – 80°CA aTDC range was summed over the frequency range of 5 – 28 kHz. This procedure was done in real-time and allowed the adjustment of combustion phasing (via spark timing) to meet the prescribed level. Further details on the computation of KI may be found in [20].

In addition to KI, the onset of end-gas autoignition was also quantified using a method termed Trace Autoignition, which was first implemented with the current experimental engine in [20]. Inspired by work of Borg & Alkidas in [33], this method examines the decay rate of the apparent heat release rate at the end of the combustion event, quantified as min(dAHRR/d°CA). An increase in the absolute value of min(dAHRR/d°CA) correlates well with an increase in end-gas autoignition magnitude, which rapidly concludes the combustion event. An illustration of this is provided in Figure A1, which plots the AHRR against phasing for 250 cycles, and highlights the calculation of the min(dAHRR/d°CA) value for an advanced, lightly autoigniting cycle. Figure A2 shows best-fit lines fitted to the cycles with absolute values of min(dAHRR/d°CA) which are elevated due to autoignition, and those at the baseline value. The intersection of these two best fit lines represents the CA50 needed for trace autoignition of a given operating condition.

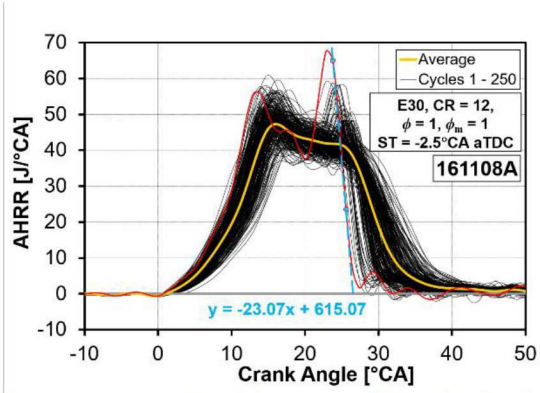

Figure A1. Apparent Heat Release Rates of 250 cycles plotted against engine phasing (crank angles). The average AHRR is shown in yellow, while an advanced, lightly autoigniting cycle is shown in red, with a line fitted to the AHRR decay at the end of combustion.

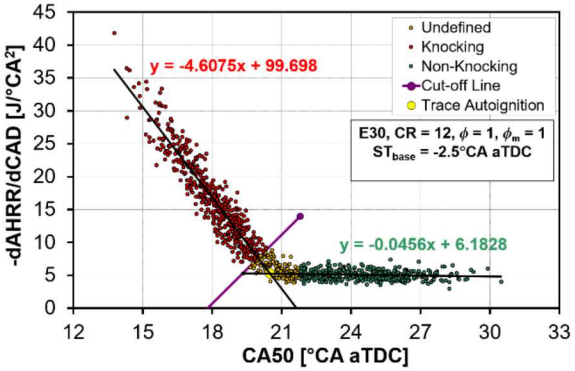

Figure A2. AHRR decay rate for 1000 cycles, with best-fit lines illustrating the determination of trace autoignition.

Appendix B: Predicted sensitivity of end-gas autoignition timing to diluent addition

As a preliminary study to probe the effect of diluent addition on autoignition characteristics, a two-zone model for a spark-ignition engine in CHEMKIN was utilized. The two zone model solves for the coupled evolution of thermodynamic properties of each zone, namely a burned and unburned zone, corresponding to the mass behind or ahead of the flame front, respectively. In the two-zone model the heat-release rate associated with flame propagation is prescribed, rather than calculated, while the composition of the unburned zone is governed by kinetic rates. When the chemistry predicts that the unburned zone undergoes autoignition, the model assumes that all of the mass in the unburned zone autoignites, causing a sudden rise in the predicted pressure.

The baseline conditions of the Alkylate and E30 fuels at CR = 12 were replicated first, and then a small fraction of CO_2 (3% of initial air mass) was introduced to probe the effect of diluent addition on the autoignition in the unburned zone. The simulation was initialized at the intake-valve closure timing. Initial values of temperature, pressure, and compositions were taken from the experimental data. The burn rate computed from the experimental data was imposed to model the deflagration process.

Figure B1 shows the change in the in-cylinder pressure traces when CO_2 is added to the baseline conditions for the E30 and Alkylate fuels. Both fuels experience retarded autoignition timing with the addition of CO_2, as evidenced by the retarded pressure rise visible in Figure B1. It is also possible to see a different sensitivity to the CO_2 dilution in the shifting autoignition timing. For the first-order estimation of change in autoignition timing with further addition of diluent, linear extrapolation was conducted and compared with the experimental result. In Fig. B2, the result of the linear extrapolation based on the simulation results is plotted in an inverted axis. This is because in the actual experiment, the combustion phasing is advanced until it becomes knock-limited. When the combustion phasing is advanced, high pressures and temperatures are reached earlier in the cycle. This results in the advancement of the autoignition timing from that of the baseline condition. For the comparison presented here, it is simply assumed that the retard of predicted autoignition timing is comparable to the advancement in the measured autoignition timing.

Figure B2 illustrates that for the Alkylate fuel, extrapolation based on the small compositional perturbation successfully predicts the impact of CO_2 dilution on change in autoignition timing. Figure B2 also shows that CO_2 dilution has a greater impact on the E30 fuel, indicating that this simplistic approach can capture some of the effects observed from the experiment. However, the simulation was conducted without consideration of the impact of dilution on the deflagration-based burn rate, which will change in the experiment as depicted in Figure B3. When the combustion phasing changes, the temperature and pressure histories of the end-gas change accordingly and the amount of time spent in each temperature regime will change as well. Figure B4 and B5 illustrates the estimated reactant temperature history and the residence time in various temperature regimes for the E30 fuel, undiluted and CO_2-diluted condition. The residence time in temperature regimes above 800 K shows significant differences, strongly reducing the time spent in the 800-900 K range when CO_2 is added.

In order to correctly capture the combinations of complex phenomena affecting the autoignition characteristics at a given conditions, the simplistic approach based on sensitivity analysis using small perturbation of a 2-zone model cannot be used. Instead, it is necessary to supply not only the appropriate initial pressure and temperature, but also the burn rate which corresponds to the case to be studied. Such procedure is not different from assigning the experimentally obtained boundary conditions to the closed reactor. It was also found that despite the simplicity of imposing the experimentally obtained pressure traces to the closed reactor model, evolution of temperature, density, and chemical species estimated by this approaches matched with negligible error to that of a two-zone model. This indicates that even though a closed reactor model does not consider the change in mass of end-gas like in a two-zone model, it can adequately capture the evolution of thermodynamic properties and chemical species that lead to autoignition. Thus, instead of utilizing the two-zone model, the pressure traces obtained from the experiment were imposed directly on a single homogeneous reactor in CHEMKIN. Consequently, this approach does not dissect the contribution of each effect discussed above, but rather allows studying autoignition fundamentals (including the effect of thermal stratification) for conditions that encompass the effects of diluents on deflagration heat release and changes to the combustion phasing.

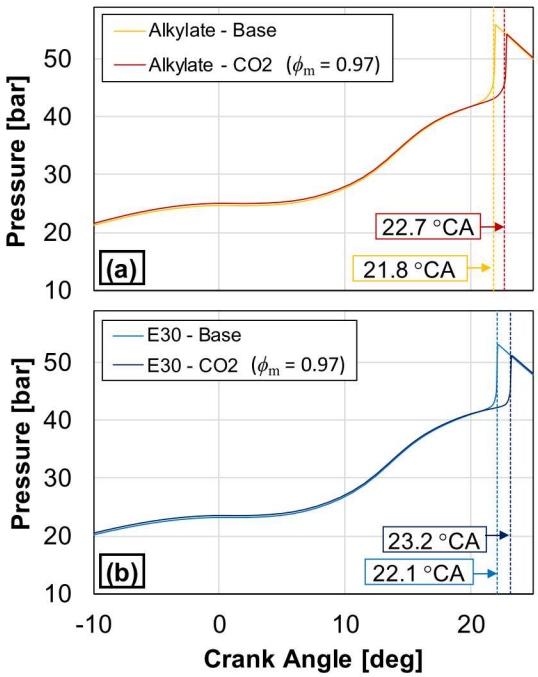

Figure B1. Pressure histories predicted by two zone model in CHEMKIN for (a) Alkylate and (b) E30 at CR = 12, baseline undiluted (ϕ = 1.00) condition, and also for a slightly CO_2-diluted condition with ϕ_m = 0.97. The numbers in the figure indicate the predicted autoignition timing.

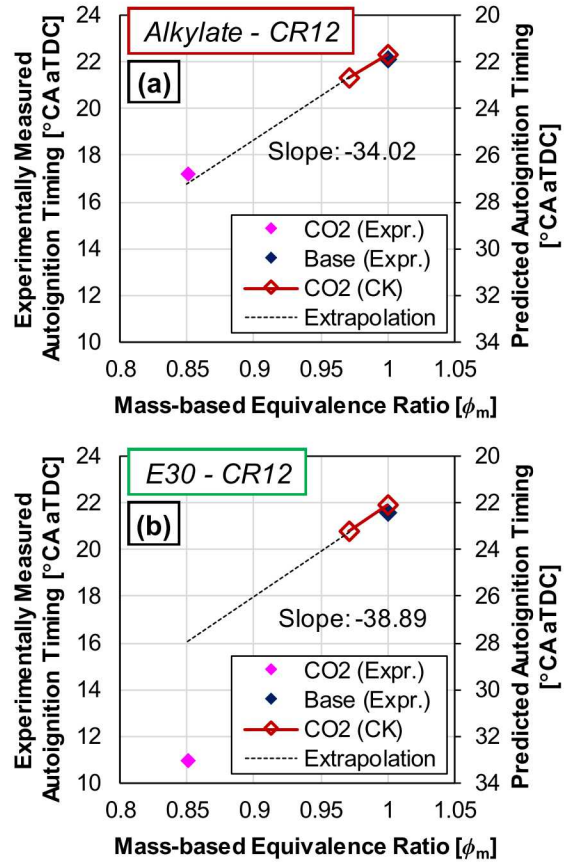

Figure B2. Comparison between the measured and the predicted autoignition timing for (a) Alkylate and (b) E30 at CR = 12. The predicted autoignition timing for higher dilution ratio is obtained from the sensitivity to diluent addition.

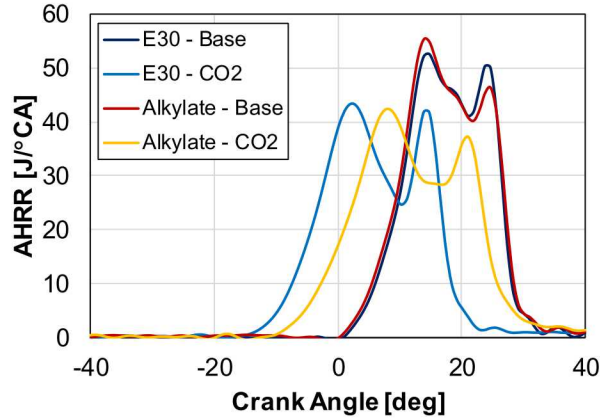

Figure B3. Experimentally measured AHRR plotted against crank-angle for the Alkylate and E30 fuel at CR = 12, undiluted (ϕ_m = 1.00) and CO_2-diluted (ϕ_m = 0.85) cases.

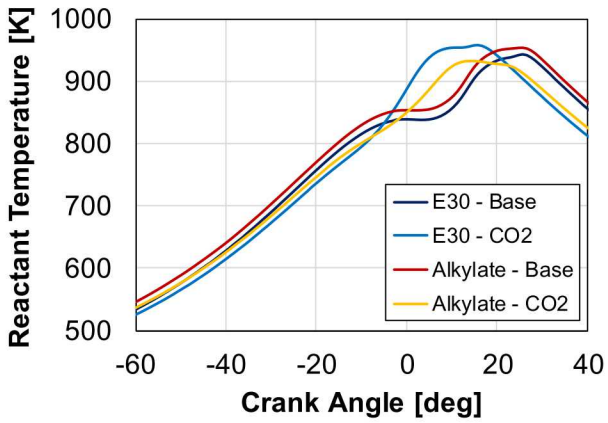

Figure B4. Isentropic temperature histories of the end-gas reactants for Alkylate and E30 fuel at CR = 12, undiluted and CO_2-diluted conditions.

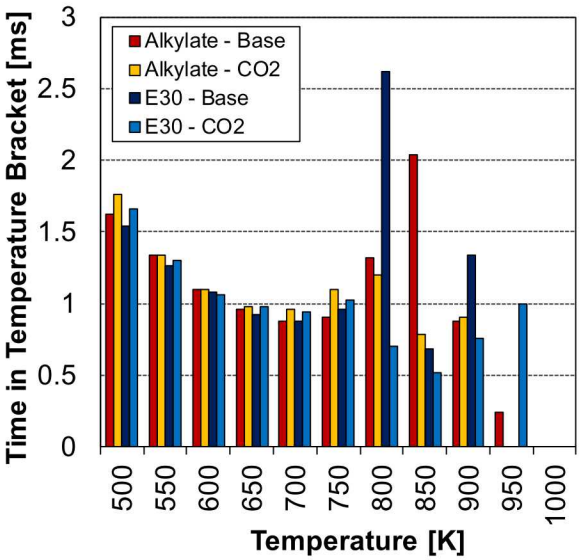

Figure B5. Residence time in 50-K wide temperature brackets for the Alkylate and E30 fuels at undiluted and CO_2-diluted conditions, corresponding to Figs. B3 and B4.

Appendix C: Quantification of the effect of uncertainty in the initial input values on prediction of autoignition timing in the adiabatic core

There are several factors that possess some degree of uncertainty: the initial temperature at the start of simulation, the local in-cylinder ϕ due to imperfect fuel-air mixing, and the response of the chemical mechanism to trace species. The surrogate formulation and the chemical mechanism itself are not perfect either. To quantify the effect of uncertainty of key parameters on the prediction of autoignition timing, the initial temperature, ϕ, and amount of NO were varied by ±5 K, ±0.04, and ±10 ppm, respectively. The additional computations were carried out for all three fuels without dilution at CR = 12. These conditions were selected because the undiluted case with High Aromatic fuel at CR = 12 shows the largest discrepancy between the measured and predicted autoignition timing, and it was deemed necessary to determine if the modeling of the High Aromatics fuel was particularly sensitive to inaccuracies in the inputs. As summarized in the last row of Table C1, the prescribed variations in the model inputs shift the predicted autoignition timing less than ±1°CA. The fuels' relatively small and uniform response to variations of input condition suggests that the larger discrepancy for the High-Aromatic fuel under CR = 12 undiluted conditions should be attributed to some other deficiency in the model.

Table C1. Summary of deviations of model relative to the experiment, experimental cycle-to-cycle variability, and response of model to input variability for CR = 12, baseline non-diluted cases.

[°CA]	Alkylate	High Aromatic	E30
$\tau_{ig,exp} - \tau_{ig,sim}$	0.34	2.95	0.60
σ of $\tau_{ig,exp}$	0.93	0.85	0.84
Variations in $\tau_{ig,sim}$	-0.89 to 0.98	-0.83 to 0.87	-0.89 to 0.98